

Multimodal Optical Feature Extraction with a Free-Space Photonic Extreme Learning Machine

Anushka Kumari^{1,*}, Anushree Khisti^{1,*}, Abhinav Choube^{1,2,*}, Devansh Satra¹, Srivatsa Murali¹, and Anshuman Kumar^{*1}

¹Laboratory of Optics of Quantum Materials, Department of Physics, Indian Institute of Technology Bombay, Mumbai 400076, India

²Department of Physics and Electronics, Institute for Excellence in Higher Education, Bhopal 462042, India

*These authors contributed equally.

Abstract

Photonic extreme learning machines (PELMs) replace a digitally trained hidden layer by a fixed optical transformation, allowing a high dimensional feature map to be generated by physical propagation while only the final readout is learned. Existing free-space PELM demonstrations have established this principle for image and tabular benchmarks, but a unified multimodal optical feature extractor spanning structurally different data types has remained largely undeveloped. Here we demonstrate a single free-space PELM platform for image, audio derived, binary tabular, and regression tasks using phase only SLM encoding, Fourier like free space propagation, and camera intensity detection. The same optical apparatus achieves 96.56% accuracy on MNIST, 95.67% on spoken digit audio from log-Mel spectrograms, 100.00% on Mushroom classification, and 0.0699 NRMSE on Abalone regression. To our knowledge, this is the first free space PELM spanning image, audio derived, and tabular tasks in one physical pipeline, and the first PELM implementation of spectrogram based spoken digit classification. Empirical distance preservation and kernel alignment diagnostics reveal two operating regimes: geometry preserving for image and regression tasks, and distributed class mean accumulation for audio derived spectrograms. These results establish multimodal PELMs as a practical route toward general purpose optical machine learning.

1 Introduction

Optical computing has emerged as a serious hardware direction for machine learning because the elementary operations required by modern learning systems, including high-dimensional linear mixing, convolution, projection, and feature expansion, are naturally implemented by interference, diffraction, and propagation. Several distinct photonic machine learning platforms have therefore been developed. Programmable Mach-Zehnder interferometer meshes and coherent nanophotonic circuits implement trainable or programmable linear transformations on chip [1–5]. Diffractive optical neural networks use spatially engineered passive layers to implement trained free-space transformations [6, 7], while on chip diffractive photonic processors extend the diffractive computing idea to integrated photonic tensor and graph processing architectures [8, 9]. Integrated photonic tensor cores and wavelength multiplexed processors exploit microcombs, phase change materials, non volatile photonic memories, and high speed modulation to accelerate convolution and matrix vector operations [10–13]. Photonic reservoir computers use multimode propagation, delay systems, speckle dynamics, or nonlinear optical nodes as fixed dynamical reservoirs with a trained electronic readout [14–16]. Recent work has also begun to explore multimodal and on-chip training paradigms in photonic neural networks [17–19]. Broader reviews have emphasized that optical inference can be performed through deeply different physical mechanisms, ranging from coherent integrated photonics to deep optics, computational imaging, and neuromorphic photonics [20, 21].

*anshuman.kumar@iitb.ac.in

Despite this progress, many photonic neural networks remain difficult to deploy as general purpose laboratory scale learning systems. Interferometric meshes require precise calibration of many phase shifters. Diffractive networks require task specific design of physical or virtual diffractive layers. Phase change and resonator based processors are powerful but depend on integrated fabrication and device level control. Photonic reservoir computers avoid full end to end training, but recurrent or dynamical implementations often require careful temporal encoding and may be naturally suited to time-series tasks rather than arbitrary static modalities. These considerations motivate a complementary question: how far can one go with an extremely simple optical feature extractor consisting only of a phase encoder, free-space propagation, spatial filtering, and a camera?

Extreme learning machines (ELMs) provide the algorithmic framework for this question [22]. An ELM maps data to a high dimensional hidden representation using fixed random or structured weights, and only the final linear readout is trained. The optical analogue is a photonic extreme learning machine (PELM), in which the hidden feature map is produced physically. Pierangeli et al. [23] demonstrated a free-space PELM in which an SLM phase encodes the input and an embedding mask, lens propagation generates the optical mixing, camera intensity supplies the nonlinear features, and ridge regression learns the readout. That work established that free-space propagation can compete with digital kernel machines on image and tabular benchmarks without nanofabricated optical networks or optical backpropagation.

The present work advances the PELM framework in multiple directions. First, we demonstrate a single free-space PELM pipeline across genuinely distinct data modalities: MNIST image classification, spoken digit audio classification from log-Mel spectrograms, Mushroom binary tabular classification, and Abalone tabular regression. ELMs have been applied digitally to many individual data types, and photonic reservoirs have been used for temporal waveform and audio related tasks [15], but to the best of our knowledge no previous free-space PELM has demonstrated image, audio derived, and tabular learning within one fixed physical optical pipeline. We are also not aware of a prior PELM implementation using Mel spectrogram phase encoding for spoken digit classification.

Second, we provide empirical feature diagnostics across all modalities. Pairwise distance preservation, centered kernel alignment (CKA), and class mean separation are measured directly from the optical reservoir outputs and used to characterize two distinct operating regimes: one in which the optical feature map preserves input geometry (MNIST, Abalone) and one in which high dimensional readout accumulates distributed class signals despite weak global distance preservation (FSDD). A detailed theoretical analysis connecting these observations to random projection theory, intensity induced quadratic features, and matched filter accumulation is deferred to a companion publication.

The resulting message is that a PELM should not be viewed as implementing a single universal kernel independent of modality. Instead, the optical hardware provides a high dimensional physical feature map whose utility depends on the interaction among input encoding, embedding mask, intensity detection, and readout. For image like and regression tasks, distance preservation and local geometry can be directly useful. For audio derived spectrograms, class structure may survive as distributed mean shifts rather than as globally preserved distances. Characterizing these two regimes empirically, and demonstrating that the same fixed hardware supports both, is the central contribution of the present work.

2 Photonic extreme learning machine architecture

2.1 ELM readout model

Let $\{(x_i, t_i)\}_{i=1}^N$ be a supervised dataset, with inputs $x_i \in \mathbb{R}^d$ and targets t_i . A conventional ELM defines a fixed nonlinear feature map $g : \mathbb{R}^d \rightarrow \mathbb{R}^M$, constructs the hidden layer matrix

$$H = \begin{bmatrix} g(x_1)^\top \\ g(x_2)^\top \\ \vdots \\ g(x_N)^\top \end{bmatrix} \in \mathbb{R}^{N \times M}, \quad (1)$$

and learns only the readout matrix β . For one hot classification targets or regression targets collected in T , the primal ridge solution is

$$\beta = (H^\top H + \lambda I_M)^{-1} H^\top T, \quad (2)$$

where $\lambda > 0$ is the ridge parameter. When it is advantageous to work in the sample dimension, the equivalent dual solution is

$$\beta = H^\top (H H^\top + \lambda I_N)^{-1} T. \quad (3)$$

Inference is then $\hat{T} = H_{\text{test}} \beta$, with the class determined by the largest output component for classification. In a PELM, $g(x)$ is not explicitly computed by a digital hidden layer; it is measured from an optical experiment.

2.2 Optical feature map

Each input is rescaled to a phase pattern and displayed on a phase only SLM. After reshaping an input into a two dimensional array x_{pq} , the displayed phase is

$$\varphi_{pq}(x) = x_{pq} + W_{pq}, \quad x_{pq} \in [0, \pi], \quad (4)$$

where W is a fixed embedding mask kept unchanged during both training and testing. The incident field immediately after the SLM is approximately

$$E_{pq}^{\text{in}}(x) = \exp[i\varphi_{pq}(x)] = \exp[i(x_{pq} + W_{pq})]. \quad (5)$$

The free-space optical path and lenses implement a structured linear mixing of this complex field. We write the sampled field at the selected camera modes as

$$u(x) = \mathcal{S}\mathcal{F}[\exp(i(x + W))], \quad (6)$$

where \mathcal{F} denotes the fourier like propagation operator and \mathcal{S} denotes spatial selection of the first diffracted order and the finite camera readout region. The camera measures intensity rather than complex field amplitude. After binning and normalization, the feature vector is

$$g(x) = \mathcal{N} \left\{ G(|u_1(x)|^2), \dots, G(|u_M(x)|^2) \right\} \in \mathbb{R}^M, \quad (7)$$

where $M = 4096$ in the reported experiments, \mathcal{N} denotes the applied feature normalization, and G is the camera response. A useful phenomenological model for the saturating response is

$$G(I) \simeq \frac{I}{I + I_s}, \quad (8)$$

with saturation intensity I_s . Even in the weakly saturated regime, the modulus square operation introduces a nonlinear transformation of the phase encoded input.

Raw camera features are preprocessed before training. First, per sample row mean subtraction removes the global background offset:

$$\tilde{G}_i = G_i - \frac{1}{M} \sum_{m=1}^M G_{im}, \quad (9)$$

where M is the total number of readout features. For kernel analysis, an additional column mean centering step is applied to remove the dataset level mean from each feature channel:

$$\hat{G}_{im} = \tilde{G}_{im} - \frac{1}{N} \sum_{j=1}^N \tilde{G}_{jm}, \quad (10)$$

where $m = 1, \dots, M$ indexes the feature dimension and the sum runs over all N training samples. Finally, hyperspherical (ℓ_2) normalization is applied to the centered features:

$$g(x_i) = \frac{\hat{G}_i}{\|\hat{G}_i\|_2 + \epsilon}, \quad (11)$$

where $\epsilon = 10^{-12}$ is a small numerical constant added for stability. This operation maps the features onto a unit hypersphere, hereby making the inner product $\langle g(x_i), g(x_j) \rangle$ correspond to the cosine similarity between two encoded inputs. This normalization also improves the numerical conditioning of the ridge regression readout. For the ridge regression readout (lambda cross validation and testing), only the per sample centering and ℓ_2 normalization steps are applied, without the additional column mean subtraction.

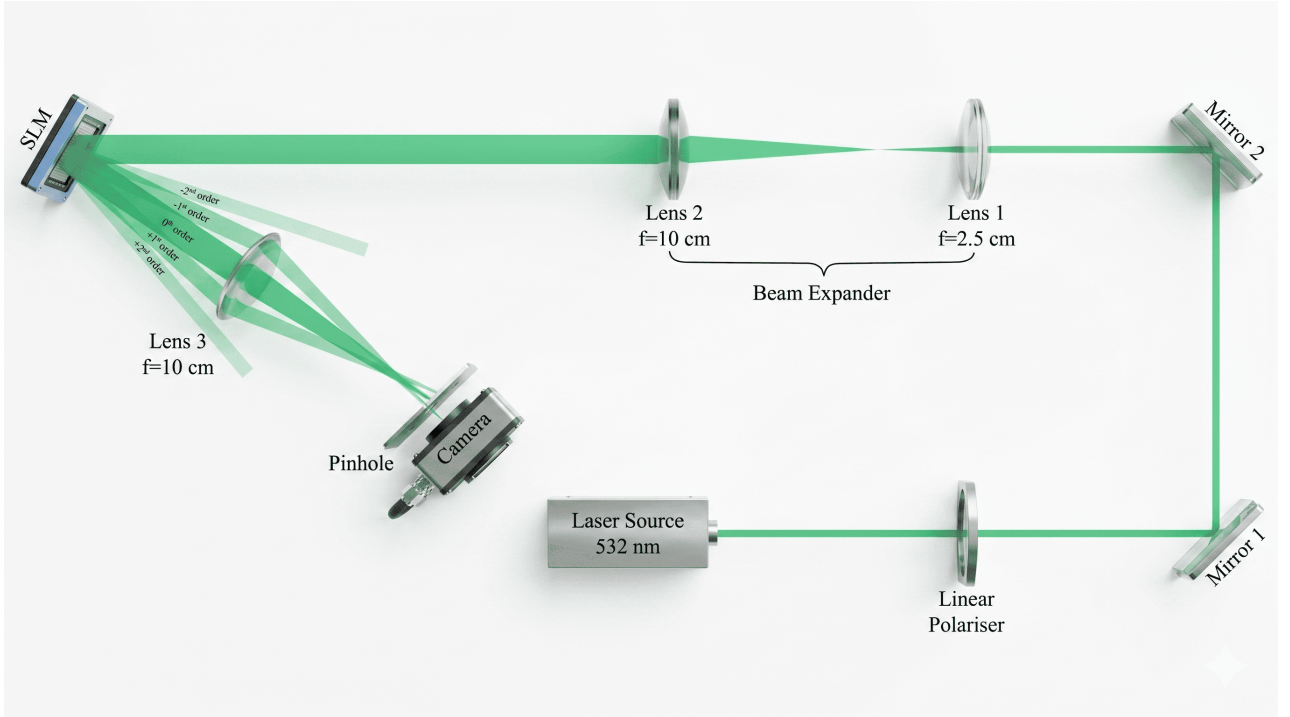


Figure 1: Experimental free-space PELM. A 532 nm laser is polarisation -controlled and phase modulated by a spatial light modulator. The optical path implements Fourier like free-space mixing, an iris selects the informative first diffracted order and suppresses the zero order background, and a camera records intensity features for the ridge regression readout.

2.3 Experimental implementation

The experimental setup consists of a green continuous wave laser, a phase only spatial light modulator (SLM), a $4f$ optical propagation system, an iris for spatial filtering, and a CMOS camera. The SLM serves both as the phase encoder and as a diffraction grating. During initial alignment, the unmodulated zero order beam produced a strong background contribution that could easily dominate the recorded camera signal if left unsuppressed. In contrast, the first diffracted order carried the phase modulated information and generated a substantially richer speckle like intensity distribution. As a result, both the iris aperture and the polarizer orientation became important alignment parameters throughout the experiments.

Camera frames were converted into $M = 4096$ readout features by selecting a central region of interest and binning local 10×10 pixel blocks into a 64×64 feature grid. Although the camera sensor has a native resolution of 1440×1080 pixels, only a cropped region of 1280×1024 pixels was used during processing. This cropping was necessary because the optical field followed an approximately Gaussian intensity profile, leaving pixels near the sensor edges weakly illuminated or completely dark.

Including these regions artificially lowered the average frame intensity and distorted the measured saturation statistics. Before ridge regression, feature normalization was applied to reduce sensitivity to laser, camera response fluctuations, and overall intensity variation. Over long acquisition runs, stable operation additionally required continuous camera streaming, careful bit depth scaling, and sufficient liquid crystal settling time after each SLM update. Reducing the settling interval from 0.10 s to 0.05 s consistently degraded classification performance, likely because the liquid crystal phase state was not fully relaxed.

3 Encoding strategies and multimodal protocol

3.1 Noise embedding

The baseline embedding is a random phase mask

$$W_{pq}^{\text{noise}} \sim \mathcal{U}(0, \rho), \quad (12)$$

optionally with a finite spatial correlation length set by block wise or smoothed disorder. This mask plays the role of a fixed random bias or fan in matrix. It breaks symmetries of the pure Fourier transform, lowers coherent artifacts, and increases the effective rank of the optical feature map.

3.2 Fourier embedding

As an alternative to using purely random phase noise, the free space PELM can also employ a Fourier based embedding strategy. Instead of introducing only a single spatial frequency component, this method adds a broadband spatial carrier composed of multiple frequency components to the input phase pattern. The embedding mask is generated by summing N_f discrete spatial frequencies along a fixed direction, where each component is assigned a random phase offset $\phi_n \sim \mathcal{U}(0, 2\pi)$:

$$W_{pq}^{\text{Fourier}} = \text{Arg} \left[\sum_{n=1}^{N_f} \exp \{i [2\pi n(X_{pq} + Y_{pq}) + \phi_n]\} \right], \quad (13)$$

with (X_{pq}, Y_{pq}) representing the normalized spatial coordinates of the SLM.

Introducing this directional carrier shifts the modulated optical field away from the optical axis, allowing the information carrying first diffracted order to be more cleanly separated from the unmodulated zero order background. Compared with the fully stochastic noise mask, the Fourier embedding imposes a more structured and multi-periodic phase modulation during optical mixing. This increases the spectral richness of the resulting phase mask and, in turn, broadens the effective dimensionality of the optical feature space

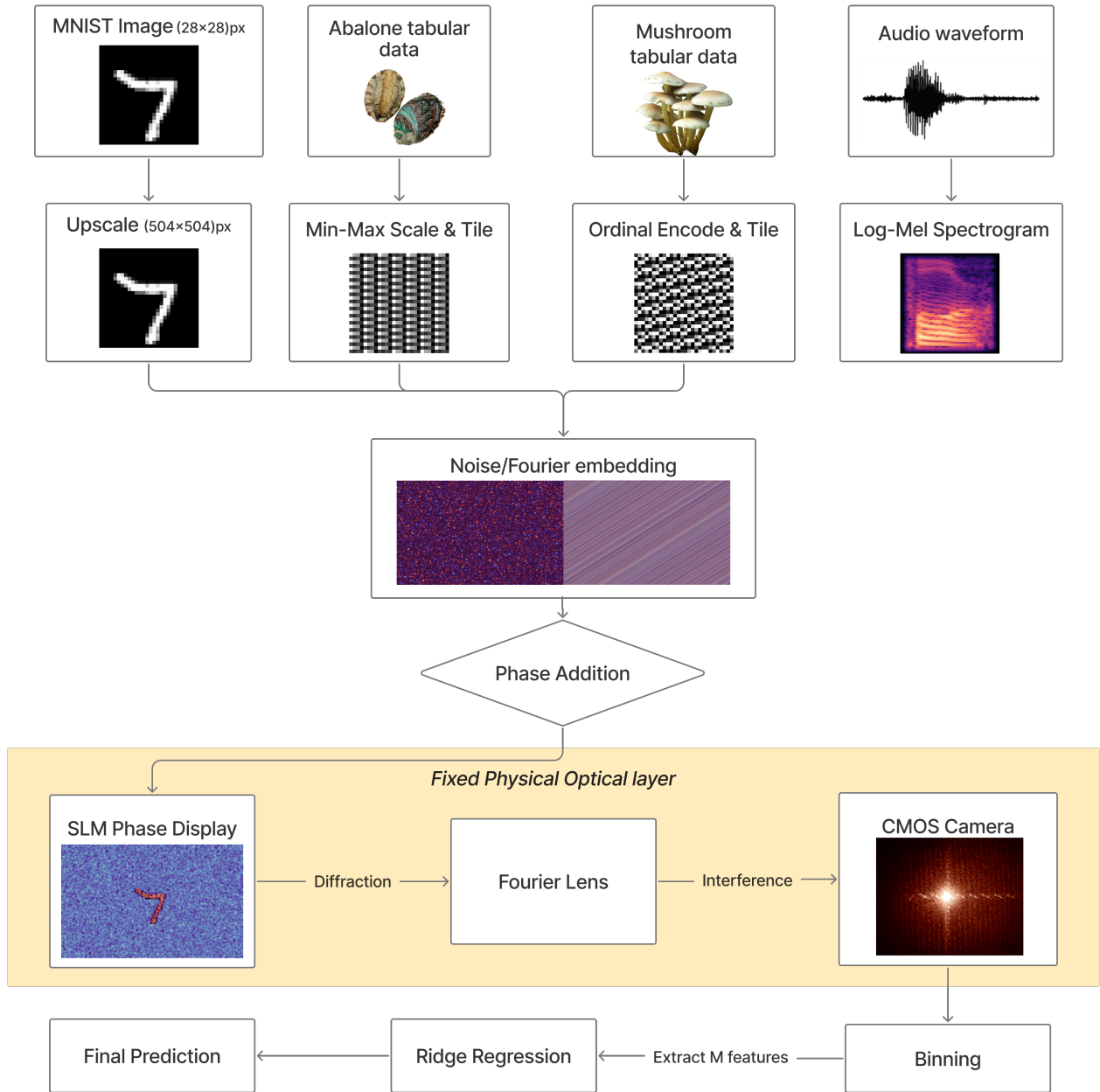


Figure 2: Overview of the multimodal PELM pipeline used in this work. Image data, audio derived spectrograms, and tabular inputs are first converted into phase patterns for SLM display and then combined with fixed embedding mask. The encoded optical field undergoes free space propagation, after which the resulting intensity patterns are captured by the camera and converted into feature vectors. Only the final readout layer is trained digitally, while the optical transformation itself remains fixed

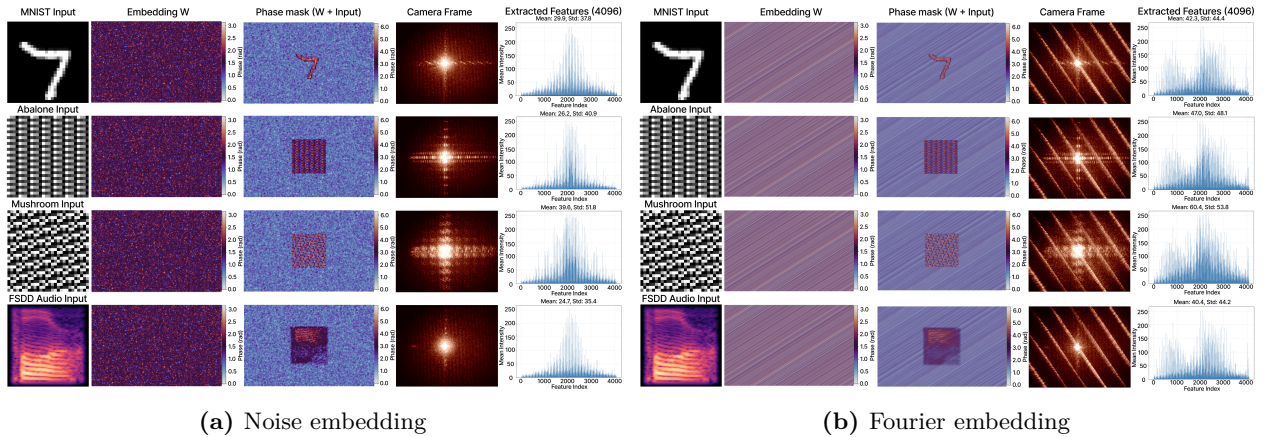


Figure 3: Comparison of the two optical encoding approaches used in the experiments: (a) noise embedding and (b) Fourier embedding. Each row illustrates a representative stage of the pipeline, including the original input pattern, the corresponding phase mask displayed on the SLM, and the resulting camera recorded intensity distribution after optical propagation.

3.3 Datasets

Four datasets representing different data modalities were evaluated in this work. MNIST was used as the primary image classification benchmark and consists of 60,000 training images together with 10,000 test images distributed across ten handwritten digit classes. Each grayscale image has a spatial resolution of 28×28 pixels, making it well suited for direct optical phase encoding and free-space propagation experiments.

The Free Spoken Digit Dataset (FSDD) [24] was employed as an audio classification task. The dataset contains 3,000 spoken recordings of digits 0 - 9, sampled at 8 kHz, with individual recordings typically ranging from 0.5 to 1 second in duration. Audio recordings were converted into log-Mel spectrogram representations before phase encoding, following the use of Mel scale spectral representations in speech processing [25], thereby forming a ten class audio derived classification task. For the experimental runs, 2,700 recordings were used for training, and remaining 300 recordings for final performance evaluation, with balanced class distributions across all spoken digits.

The Mushroom dataset [26] was used as a binary classification task to distinguish edible from poisonous mushrooms based on 22 categorical tabular attributes describing mushroom characteristics such as cap shape, cap surface, cap color, bruising, odor, gill attachment, gill spacing, stalk shape, habitat, and population type. Of the original 8,124 samples, 2,480 samples containing missing stalk root information were excluded, yielding 5,644 valid records. Since the dataset consisted entirely of categorical attributes, each feature was encoded independently using deterministic per feature categorical index encoding to preserve category identity without introducing artificial ordinal relationships. The encoded features were subsequently min-max scaled to the range $[0, 255]$ and tiled into 28×28 two dimensional spatial representations for optical phase modulation. The valid records were then divided into a training set of 4,124 samples and a testing set of 1,520 samples.

The Abalone dataset [27] was used for the regression experiments and contains 4,177 samples described by eight input features related to the physical properties of abalone specimens. These features include a categorical sex label (Male, Female, or Infant), shell length, shell diameter, shell height, whole weight, shucked weight, viscera weight, and shell weight. Here, whole weight refers to the total mass of the abalone before processing, shucked weight represents the mass of the edible meat after removal from the shell, viscera weight corresponds to the internal organ mass, and shell weight denotes the dry shell mass after processing. The regression target is the number of shell rings, which is commonly used as an approximate estimate of abalone age. The dataset was divided into 3,480 training samples and 696 testing samples, corresponding to an approximate 80/20 split.

To maintain compatibility with the optical processing pipeline, nonimage inputs were reshaped or tiled into two dimensional phase patterns before being displayed on the spatial light modulator (SLM). The same free space propagation setup and readout training procedure were then used

across all datasets to ensure a consistent framework. The regularization parameter λ was optimized independently for each dataset using validation based hyperparameter sweeps.

4 Experimental Results

The experimental performance was evaluated across two embedding strategies: the random noise embedding and the Fourier embedding. For both strategies, the ridge regularization parameter λ (Eq. 2) was optimized independently for each dataset by a logarithmic grid search sweeping λ from 10^{-5} to 10^1 . The optimal λ was selected using cross validation performance on the training split, highest accuracy for classification tasks (MNIST, FSDD, Mushroom) and the lowest NRMSE for regression (Abalone). The optimal λ values are dataset dependent and reflect the interaction between the optical feature geometry and the ridge readout; the test set was held out throughout and evaluated once after final model selection. The close agreement between cross validation and test performance across all datasets (Table 1) confirms that the selected λ values do not lead to overfitting.

Table 1 summarizes the optimized classification results. For each dataset, the reported accuracy corresponds to the best value obtained over the λ sweep, with the corresponding value of λ shown explicitly. The comparison to earlier free-space PELM work is not included as a table column, since the goal here is to establish a unified multimodal optical feature extraction framework rather than to frame the work as a direct benchmark against a single previous implementation. Nevertheless, to the best of our knowledge, the MNIST accuracy reported here is among the highest, reported for a free-space PELM architecture using an SLM camera optical reservoir and a trained linear readout.

Table 1: Optimized experimental performance of the free-space PELM. The ridge parameter λ was swept independently for each dataset and embedding. Both the noise and Fourier embeddings achieve comparable performance across all datasets, with the Fourier embedding providing a small but consistent improvement in most cases. The best classification accuracies obtained with the Fourier embedding are 96.56% on MNIST, 95.67% on FSDD spoken digits, and 100.00% on Mushroom classification, while the regression performance on Abalone remains within a small difference in NRMSE between embeddings.

Dataset	Task	Embedding	Best λ	Test performance	CV performance
MNIST	10 class handwritten digit classification	Noise	7.278×10^{-4}	96.35% accuracy	95.86% accuracy
MNIST	10 class handwritten digit classification	Fourier	7.278×10^{-4}	96.56% accuracy	96.46% accuracy
FSDD	10 class spoken digit classification from log-Mel spectrograms	Noise	1.887×10^{-3}	93.00% accuracy	91.56% accuracy
FSDD	10 class spoken digit classification from log-Mel spectrograms	Fourier	1.887×10^{-3}	95.67% accuracy	95.22% accuracy
Mushroom	Binary tabular classification	Noise	1.00×10^{-5}	100.00% accuracy	100.00% accuracy
Mushroom	Binary tabular classification	Fourier	1.00×10^{-5}	100.00% accuracy	100.00% accuracy
Abalone	Tabular regression	Noise	4.89×10^{-3}	0.0699 NRMSE	0.0770 NRMSE
Abalone	Tabular regression	Fourier	4.89×10^{-3}	0.0704 NRMSE	0.0768 NRMSE

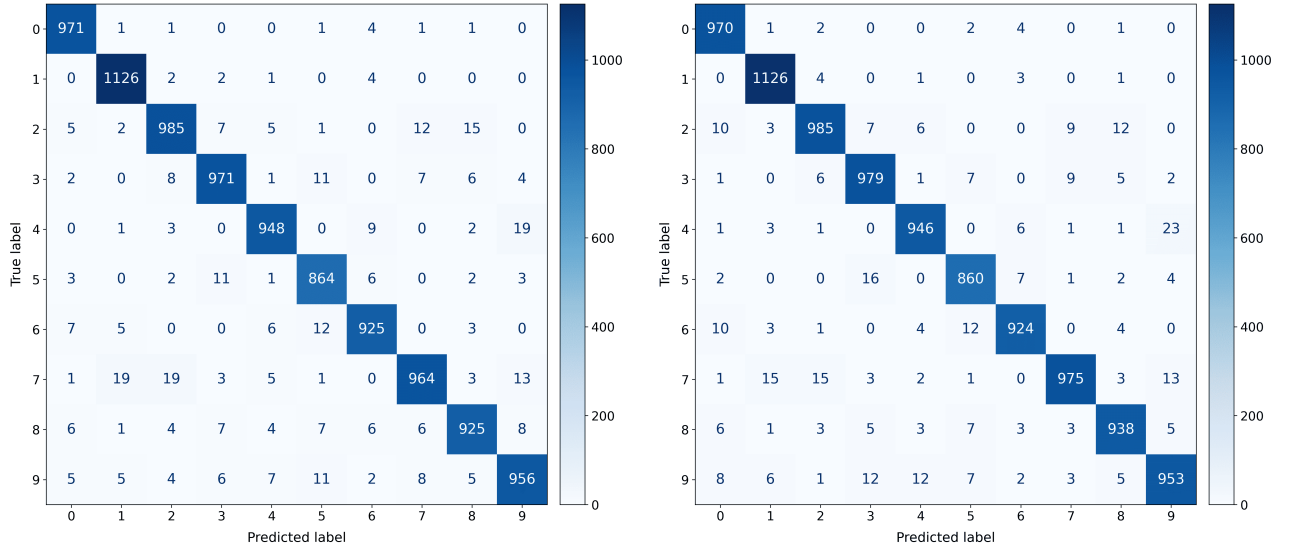
The MNIST experiments show that the optical feature map remains highly effective on a large scale image classification benchmark. After optimizing the ridge regularization parameter λ , the PELM achieved a test accuracy of 96.35% using the noise embedding and 96.56% using the Fourier embedding.

A similar pattern was observed across the other datasets, where the difference in performance between the two embeddings remained relatively small. In most cases, the variation was within 1 - 2% for classification accuracy and only a few thousandths in NRMSE for regression tasks. These results

suggest that both embeddings generate strong optical feature representations, although the Fourier embedding consistently provides a slight performance advantage across most benchmarks.

For MNIST, the corresponding cross validation (CV) accuracies were 95.86% for the noise embedding and 96.46% for the Fourier embedding. The close agreement between CV and test performance indicates that the model generalizes consistently across validation folds rather than benefiting from a favorable train test split. During hyperparameter optimization, the CV scores were computed using 5 fold cross validation. The training set was divided into five folds, with four folds used for training and the remaining fold used for validation in each run . The final CV accuracy was obtained by averaging the validation performance across all folds. StratifiedKFold was used for classification datasets to preserve class balance within each split, while standard KFold was used for regression experiments.

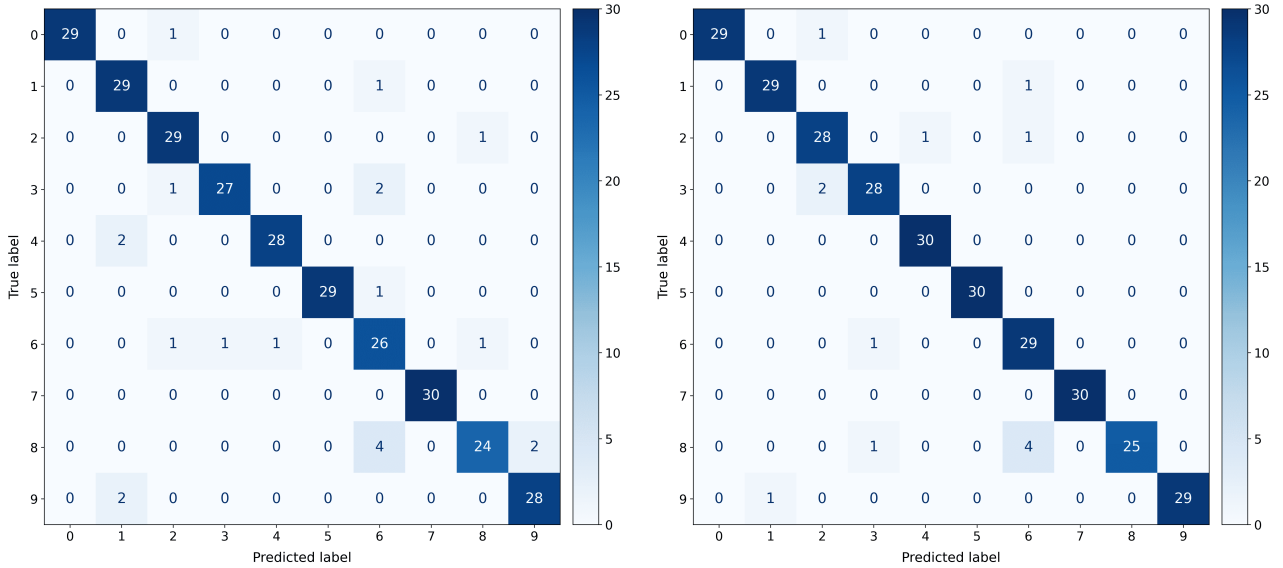
The confusion matrices shown in Fig. 4 further shows that both embeddings maintain a strongly diagonal classification structure. However, the Fourier embedding produces slightly fewer off diagonal digit confusions, indicating a slight improvement in class separability within the optical feature space.



(a) Noise embedding, 96.35% test accuracy, CV accuracy 95.86%, best λ is 7.278×10^{-4} . (b) Fourier embedding, 96.56% test accuracy, CV accuracy 96.46%, best λ is 7.278×10^{-4} .

Figure 4: MNIST confusion matrices obtained after optimizing the ridge regularization parameter λ . Both embeddings produce a strongly diagonal classification structure, showing reliable digit recognition across classes. The Fourier embedding achieves slightly higher overall accuracy and shows fewer off diagonal misclassifications compared to the noise embedding, suggesting improved class separation in the optical feature space.

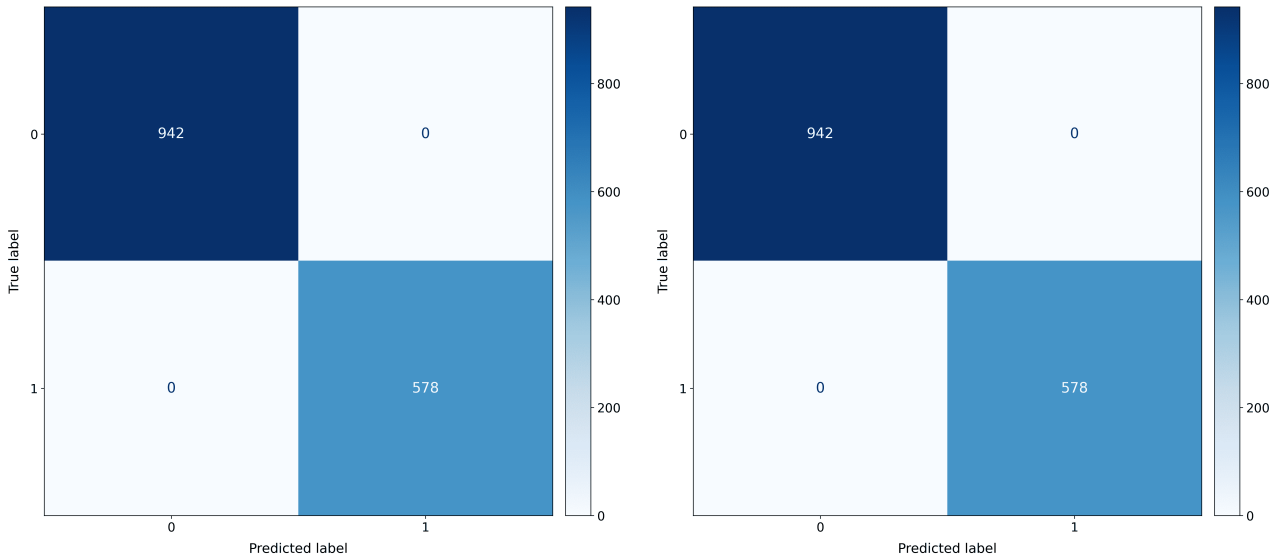
The FSDD experiment tests whether the same optical hardware can process a non-image modality. Each spoken digit is first represented as a log-Mel spectrogram and then encoded as a phase pattern on the SLM. This is a significantly different task from MNIST ,the two axes of the spectrogram represent time and frequency rather than spatial coordinates, and therefore the relation between input geometry and SLM plane geometry is less direct. Even under this encoding mismatch, the PELM reaches 93.00% accuracy with noise embedding and 95.67% accuracy with Fourier embedding. This result is one of the central multimodal findings of the work. It shows that free-space optical propagation can extract discriminative features not only from spatial image data but also from audio derived time frequency representations.



(a) Noise embedding, 93.00% test accuracy, CV accuracy 91.56%, best $\lambda = 1.887392 \times 10^{-3}$. (b) Fourier embedding, 95.67% test accuracy, CV accuracy 95.22%, best $\lambda = 1.887 \times 10^{-3}$.

Figure 5: FSDD spoken digit confusion matrices after optimizing the ridge parameter. The PELM performs ten class audio derived classification using log-Mel spectrograms encoded as optical phase patterns. The Fourier embedding improves the accuracy to 95.67%.

The Mushroom dataset provides a binary tabular classification benchmark. Since the task is nearly linearly separable after suitable encoding, both embeddings perform close to saturation. Both the noise and Fourier embeddings reach 100.00% classification. The excellent performance indicates that the optical feature map does not degrade tabular class information when the categorical features are encoded into a stable phase representation. At the same time, the strong dependence on the ridge parameter shows that for smaller tabular datasets, readout regularization can be as important as the optical embedding itself.



(a) Noise embedding, 100%, best $\lambda = 1.00 \times 10^{-5}$. (b) Fourier embedding, 100%, best $\lambda = 1.00 \times 10^{-5}$.

Figure 6: Mushroom binary classification confusion matrices after optimizing the ridge parameter λ . Both embeddings achieve 100.00% classification accuracy, indicating that the optical feature map preserves the separability of the tabular features extremely well.

Across all three classifications, the Fourier embedding provides performance comparable to or slightly better than the noise embedding after optimizing λ . This trend suggests that structured

spectral embeddings can provide a more useful optical feature basis than purely random phase disorder for the present SLM camera PELM configuration. Importantly, the improvement is observed across image, audio derived, and tabular data, supporting the view that the embedding mask should be treated as a central design rather than as a minor experimental detail. The physical origin of this behavior, and its relationship to prior reports on random optical embeddings, remains under investigation.

The Abalone benchmark is a regression task; its optimized performance is reported using the normalized root mean square error in Table 1.

The full λ optimization curves for all reported datasets and embeddings are provided in the Supplementary Information, Sec. B. These sweeps show that the optimal regularization strength is dataset dependent: MNIST is relatively stable over a broad range of λ , whereas smaller tabular and audio derived datasets exhibit sharper optima.

5 Empirical feature space diagnostics

In this paper, we focus on the experimental evidence for multimodal optical feature extraction rather than presenting a complete mathematical theory of the mechanism. A detailed theory of distance preservation, kernel formation, and high dimensional readout accumulation is being developed and will be reported in a subsequent publication. Here, we restrict ourselves to directly measured diagnostics obtained from the optical feature matrices: pairwise distance preservation, kernel alignment, class separation metrics, and low dimensional feature visualizations. These diagnostics provide an empirical view of how the same free-space PELM hardware supports image, audio derived, tabular classification, and regression tasks.

For each input x_i , the optical system produces a normalized feature vector $g(x_i) \in \mathbb{R}^M$, where M denotes the number of binned camera readout channels. The diagnostics in this section compare the structure of the original input representation with that of the experimentally measured optical feature representation. To ensure computational tractability and reduce class imbalance bias, these diagnostics were evaluated on controlled subsets of the training data. Pairwise distance preservation analysis was computed using 50 random samples across all datasets to optimize scatter plot legibility. Centered kernel alignment (CKA) and class separation metrics were evaluated on class balanced subsets (20 samples per class) for discrete classification datasets. Conversely, the continuous target manifold of the Abalone regression task was evaluated using an expanded random subset of 2000 samples; this high density pool is mathematically required to maintain proper target density across its integer milestones, preventing metric sparsity and ensuring a stable median distance heuristic during continuous auto RBF kernel construction. Unless stated otherwise, the main text diagnostics are shown for the Fourier embedding, which achieved the strongest optimized performance across the classification benchmarks in Sec. 4. The corresponding diagnostics for the noise embedding are provided in the Supplementary Information.

5.1 Experimental optical kernel characterization

Before evaluating the task specific utility of the optical feature space, we first verify the fundamental mathematical operation executed by the physical hardware. The intensity detection process of the PELM is theoretically predicted to implement a nonlinear kernel governed by the angular geometry of the encoded inputs. To test this, we experimentally measured the empirical optical kernel from raw pairwise feature similarities and compared it against several exact double centered theoretical kernels. These include the analytical phase kernel (K_{phase}), the complex Gaussian approximation ($K_{Gaussian}$), arc cosine kernels corresponding to infinite width ReLU networks (K_1, K_2), and an angular Radial Basis Function (RBF) kernel.

As shown in Fig. 7 for the MNIST dataset using the Fourier embedding, the measured empirical kernel exhibits a strong Pearson correlation with the angular RBF, validating that the physical optics faithfully compute the expected nonlinear geometric projection. Notably, the structured spatial carrier wave of the Fourier embedding efficiently diffracts the information bearing signal away from the

unmodulated background, yielding a highly robust and well defined empirical kernel fit. The arc cosine K_2 kernel is also plotted to serve as a baseline comparison to standard digital neural networks. Because this hardware characterization proves the system naturally executes an angular RBF like projection, we adopt the angular RBF for the downstream machine learning diagnostics (such as Centered Kernel Alignment) in the subsequent sections. The kernel fit r varies across datasets and embeddings, with natural image and tabular inputs introducing confounds that suppress the measured correlation relative to the underlying empirical kernel fit, reflecting in-situ hardware kernel quality under realistic measurement conditions. The Pearson correlation of $r \approx 0.67$ obtained from natural MNIST image pairs reflects this in situ kernel fit quality. Natural images are not designed to probe the angular kernel: the binning by θ averages over many input pairs drawn from the full MNIST distribution, whose complex spatial structure and varying content introduce confounds that suppress the measured correlation relative to the true fit quality. A dedicated angular sweep experiment using purpose constructed input pairs at controlled, known angles yields $r = 0.990$ for the angular RBF kernel (see companion publication), confirming that the lower in situ value is a measurement artifact rather than a failure of the kernel model. Together, the two measurements establish that the optical hardware faithfully implements the angular RBF kernel, and Fig. 7 should be interpreted as a conservative lower bound on the true fit quality rather than a precision characterization. Full experimental kernel fits for the remaining datasets and the noise embedding are provided in the Supplementary Information (Sec. C.2).

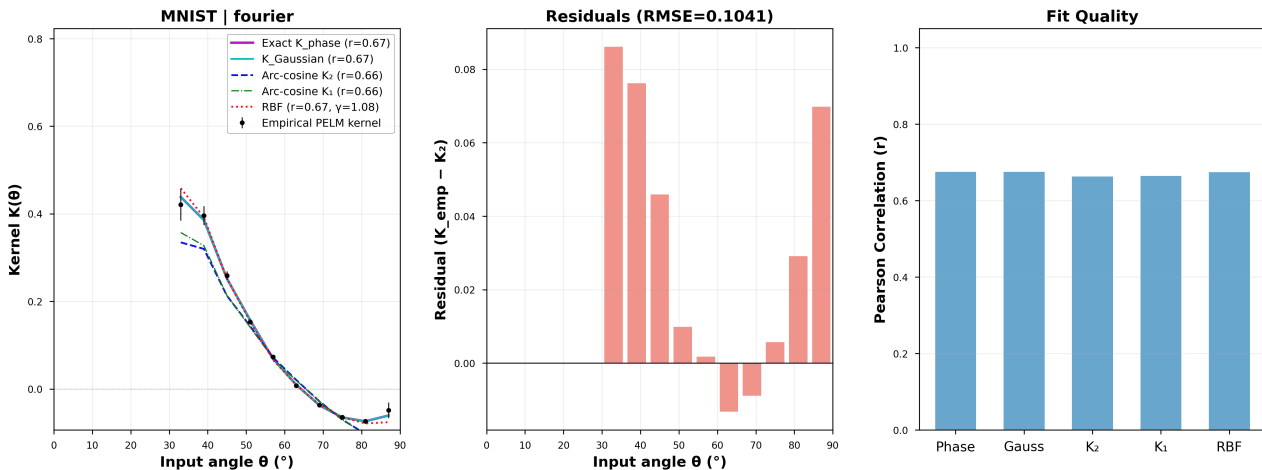


Figure 7: Experimental kernel characterization for the MNIST dataset using the Fourier embedding. The empirical PELM kernel is binned by input angle θ and compared to exact double centered theoretical predictions. The high Pearson correlation confirms that the optical hardware, aided by the structured spatial carrier of the Fourier mask, physically computes an angular RBF and K_{phase} kernel.

5.2 Relative distance structure preservation

A first diagnostic asks whether distances in the original input representation are preserved after optical propagation and camera detection. For a set of sample pairs (x_i, x_j) , we compute the original space distance

$$d_{\text{in}}(i, j) = \|x_i - x_j\|_2, \quad (14)$$

and the optical feature distance

$$d_{\text{opt}}(i, j) = \|g(x_i) - g(x_j)\|_2. \quad (15)$$

Both distance lists are standardized before plotting, and Pearson and Spearman correlations are used as empirical measures of relative distance preservation. For computational consistency across datasets, the distance-preservation diagnostics were computed using randomly selected subsets of 50 samples per dataset. This is not meant as a proof of a Johnson-Lindenstrauss type guarantee for the physical apparatus. Rather, it is a direct experimental measurement of whether the optical reservoir approximately preserves pairwise structure for each modality.

Check A: Distance Preservation in Optical Feature Space [FOURIER]

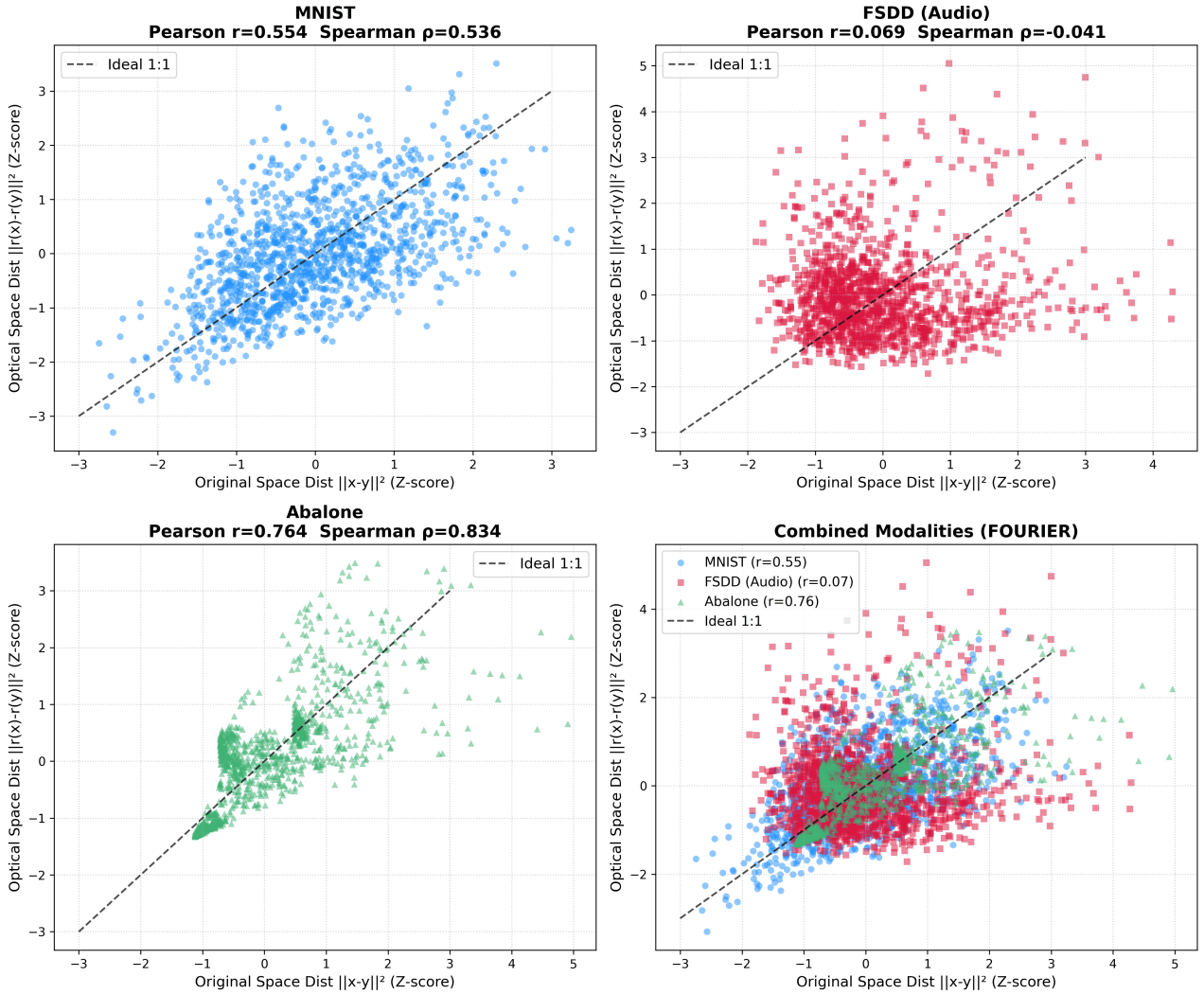


Figure 8: Empirical relative distance structure preservation for the Fourier embedding. Pairwise distances in the original representation are compared with distances in the experimentally measured optical feature space. MNIST shows moderate positive distance preservation, Abalone shows strong monotonic preservation, while FSDD shows weak global distance preservation despite high classification accuracy. The integrated panel emphasizes that a single optical feature extractor can function across various empirical regimes according to the modality.

Figure 8 reveals three separate empirical regimes. The MNIST dataset demonstrates a moderate level of positive distance preservation, indicated by a Pearson correlation coefficient of $r = 0.554$ and a Spearman rank correlation of $\rho = 0.536$. This implies that the optical feature space maintains some aspects of the geometry inherent to the original digit manifold. In contrast, the Abalone regression task exhibits significantly stronger distance preservation, with a Pearson correlation of $r = 0.764$ and a Spearman rank correlation of $\rho = 0.834$. This finding aligns our observation that the optical representation retains a continuous structure that is advantageous for regression.

FSDD shows a different behavior. The spoken digit signals are represented as log Mel spectrograms, whose axes correspond to time and frequency rather than physical spatial coordinates. When these spectrograms are encoded onto the SLM plane, global Euclidean distances in the input space are not well preserved in the resulting optical feature space. This is reflected in the FSDD panel, where Pearson correlation is $r = 0.069$ and Spearman correlation is $\rho = -0.041$. Despite this weak distance preservation, the optical system still achieves a classification accuracy of 95.67% on FSDD using the Fourier embedding. This indicates that while preserving global pairwise distances can be beneficial, it is not a strict requirement for achieving high classification performance in the PELM readout.

5.3 Kernel alignment and class separation diagnostics

To probe class structure more directly, we compute empirical kernel and separation diagnostics from the measured optical features. Kernel methods provide a natural language for comparing nonlinear feature maps [28], while kernel target alignment and centered kernel alignment quantify how well a feature space Gram matrix agrees with a target or label Gram matrix [29, 30]. We use these diagnostics empirically: they are not treated as a complete theory of PELM operation, but as quantitative summaries of how the measured optical representation organizes samples.

The linear optical Gram matrix is

$$K_{ij}^{\text{lin}} = g(x_i)^\top g(x_j), \quad (16)$$

and an RBF optical Gram matrix is constructed as

$$K_{ij}^{\text{RBF}} = \exp \left[-\gamma \|g(x_i) - g(x_j)\|_2^2 \right], \quad (17)$$

with γ fixed by the scale of the optical features. We compare these empirical kernels with the label kernel using centered kernel alignment (CKA),

$$\text{CKA}(K, L) = \frac{\langle H_c K H_c, H_c L H_c \rangle_F}{\|H_c K H_c\|_F \|H_c L H_c\|_F}, \quad H_c = I - \frac{1}{N} \mathbf{1}\mathbf{1}^\top. \quad (18)$$

In practice, feature vectors are L2 normalized before computing K^{lin} , so the linear kernel entry reduces to the cosine similarity $K_{ij}^{\text{lin}} = g(x_i)^\top g(x_j) / (\|g(x_i)\| \|g(x_j)\|)$; this follows the recommendation of Kornblith et al. [30] and makes the CKA values invariant to global intensity fluctuations in the optical measurement.

In addition to global CKA, we compute class wise separation metrics. These quantify whether a given class is better separated from the remaining samples in the measured optical feature space. The separation plots therefore test a more task specific question than pairwise distance preservation: even if the full geometry is not preserved, are the measured optical features organized in a way that the final linear readout can exploit?

For each class, separation was quantified using a Cohen’s- d style standardized separation metric,

$$S_c = \frac{\mu_{\text{within}} - \mu_{\text{between}}}{\sqrt{\frac{1}{2}(\sigma_{\text{within}}^2 + \sigma_{\text{between}}^2)}}, \quad (19)$$

where μ_{within} and μ_{between} denote the mean within class and between class similarities, respectively, and σ_{within} , σ_{between} are the corresponding standard deviations. Larger values indicate stronger class separation in the measured optical feature space.

MNIST exhibits stronger global alignment, with linear CKA = 0.3624 and RBF CKA = 0.3781, consistent with the corresponding distance preservation diagnostics. FSDD shows weaker global alignment (linear CKA = 0.2962, RBF CKA = 0.3085) despite maintaining high classification accuracy, indicating that the ridge readout can exploit class discriminative structure even when the global feature geometry appears only weakly organized.

The corresponding Mushroom diagnostics, shown in the Supplementary Information, exhibit strong binary separation. Finally, for the Abalone regression task, we employ a continuous target similarity kernel to evaluate manifold preservation, complementing the pairwise distance preservation analysis. The corresponding figures for all datasets are provided in Supplementary Section C.3.

5.4 Low dimensional feature visualizations

We further visualize the measured optical feature matrices using t-SNE [31]. These plots are not employed as standalone quantitative proof, because t-SNE has the potential to skew overall distances and is susceptible to the arrangement of local neighborhoods. Nevertheless, they offer a helpful qualitative perspective on the arrangement of high dimensional camera attributes across various modalities.

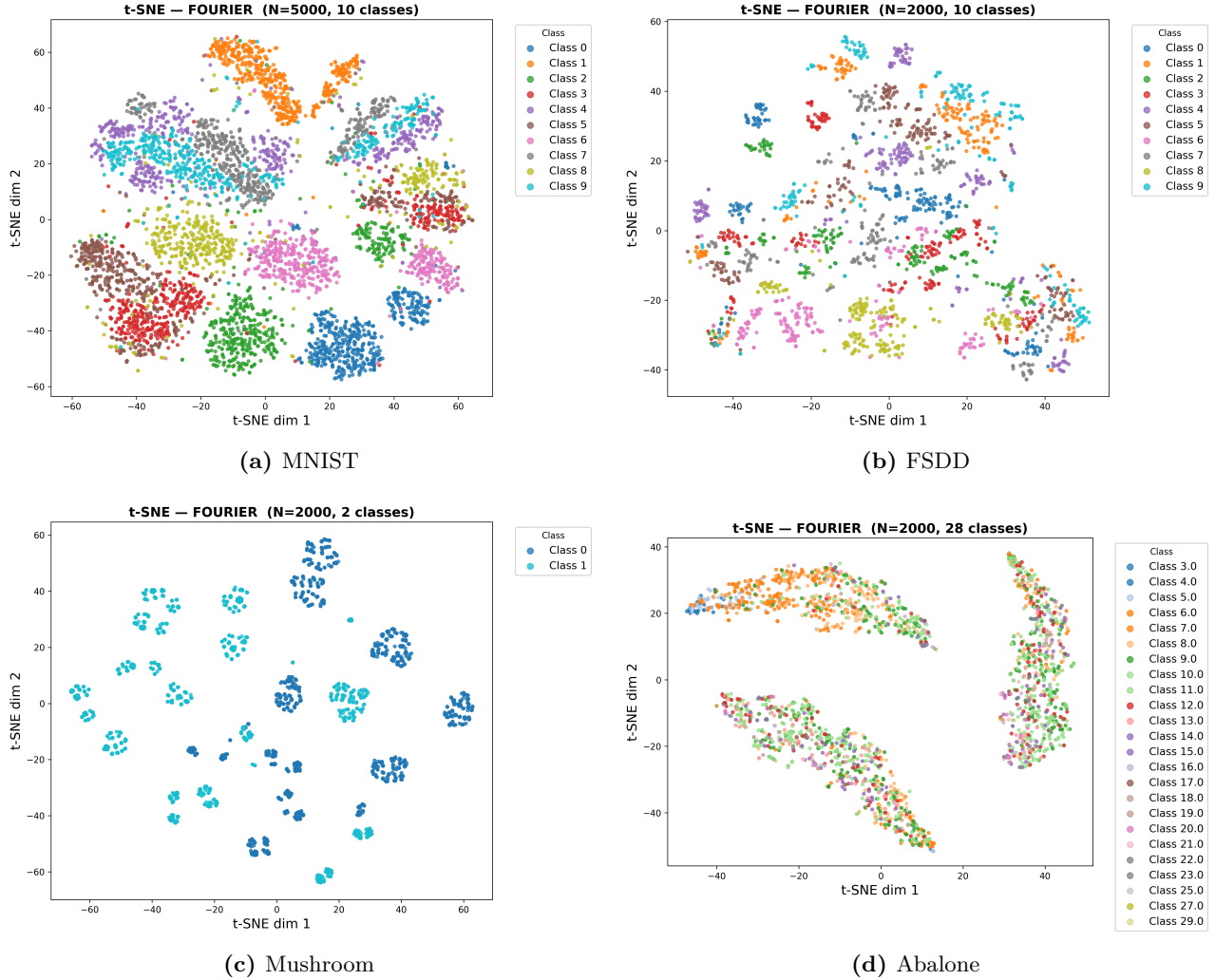


Figure 9: t-SNE graphic representations of optical characteristics that were empirically recorded for the Fourier embedding. MNIST and Mushroom demonstrate clearer class organization, whereas FSDD appears more globally blended in two dimensions, even with a strong ten class accuracy. Abalone exhibits continuous structures that depend on the target, rather than separate class clusters, aligning with its regression oriented nature.

The t-SNE visualizations illustrated in Fig. 9 strengthen the structural understandings derived from both distance preservation and CKA assessments. The MNIST dataset displays clearly defined topological groupings based on numeral digits, while the Mushroom dataset reveals apparent and linearly separated binary classifications. In contrast, the FSDD dataset seems to be more globally scattered across two dimensions, showing that its distinguishing characteristics are spread throughout the entire 4096 dimensional optical space instead of being limited to a narrow low dimensional area. Regarding the Abalone regression task, the samples are categorized by color according to specific integer target milestones related to shell rings, which range between 3.0 and 29.0. Instead of creating isolated categories, the visualization indicates a smoothly transitioning continuous structure where nearby integer targets retain close structural relationships within the latent space, visually verifying the regression maintaining attributes of the optical reservoir.

6 Discussion

The main result of this work is the experimental demonstration that a single free-space PELM can be used as a multimodal optical feature extractor. The same physical pipeline, consisting of phase only SLM encoding, free-space optical propagation, first order spatial filtering, camera intensity detection, and ridge regression readout, supports image classification, audio derived spectrogram classification,

tabular binary classification, and tabular regression. This distinguishes the present work from earlier free-space PELM demonstrations that focused on more conventional image and tabular benchmarks.

The audio result is particularly important. Log-Mel spectrograms are not native optical images; they are time-frequency representations of speech signals. The robust performance of FSDD indicates that the optical system is not simply utilizing spatial image structure. Rather, when the audio signal is incorporated as a phase pattern, free-space propagation along with intensity detection produces a high dimensional representation that encompasses sufficient class discriminative information for a linear readout.

Different modalities interact differently with the optical feature space, according to the empirical diagnostics. Measurable relative distance preservation is shown by MNIST and Abalone, suggesting that some of the input geometry survives the optical transformation. On the other hand, as optical characteristics expand, Mushroom gets closer to near separability. Despite having limited low dimensional clustering and poor global distance preservation, FSDD nevertheless retains a high degree of accuracy. Pairwise geometry preservation is helpful, but it is not the sole path to good PELM operation. This is a key finding of the manuscript.

The Fourier embedding consistently improves the optimized classification performance over the noise embedding for the completed experimental runs. This indicates that the embedding mask should be treated as a central optical design parameter rather than as a minor perturbation of the input phase. In the current work, we restrict ourselves to the completed noise and Fourier embedding experiments. More advanced embedding constructions and their detailed theoretical analysis will be addressed in future work.

In addition to the baseline preprocessing pipeline consisting of per sample DC removal, feature centering, and hyperspherical (L_2) normalization, we also explored alternative digital conditioning strategies, including power law intensity scaling and channel wise standardization. Preliminary empirical diagnostics suggest that such transformations can further improve feature space conditioning metrics, including Centered Kernel Alignment (CKA) and kernel signal to noise ratios (SNR), particularly for heterogeneous multimodal datasets. These observations indicate that the measured optical feature manifold remains amenable to additional digital conditioning prior to readout optimization. Although these advanced preprocessing techniques were not employed in the main benchmarks reported, they indicate a promising avenue for future enhancements.

Practical limitations also exist. Rather than the actual speed of light propagation, the existing system is limited by the SLM update frequency, liquid crystal settling time, camera exposure time, data transfer speeds, and environmental stability. Performance is greatly impacted by variables such as iris alignment, polarizer modifications, camera bit-depth conversion, feature normalization, and SLM settling time. These difficulties are essential for guaranteeing reproducibility and scaling towards faster optical inference, but they do not constitute conceptual constraints of PELMs.

Overall, the results suggest that free-space PELMs provide a low cost, promising framework for optical machine learning. Their benefit is in enabling high dimensional feature expansion by a passive optical transformation while retaining a simple and reliable electronic readout, rather than in replacing all digital computations. In situations where data is intrinsically optical, image like, or can be efficiently represented as two dimensional phase patterns, this hybrid optical electronic architecture is very attractive. When data are inherently visual, image like, or can be effectively represented as two dimensional phase patterns, this hybrid optical electronic structure is particularly appealing.

7 Conclusion

We have developed a multimodal free-space photonic extreme learning machine using phase only SLM encoding, Fourier like optical propagation, camera intensity detection, and ridge regression readout. With optimized ridge regularization, the system achieves 96.56% accuracy on MNIST using the Fourier embedding, 95.67% accuracy on FSDD spoken -digit classification from log-Mel spectrograms, and 100.00% accuracy on Mushroom binary classification, together with the optimized Abalone regression performance reported in Table 1. The Supplementary Information contains the complete λ optimization curves.

The empirical diagnostics show that the same optical hardware can support different learning mechanisms across modalities. Some tasks, such as MNIST and Abalone, show measurable relative distance preservation in optical feature space. Others, such as FSDD, achieve high accuracy despite weak global distance preservation, indicating that the trained readout can exploit discriminative high dimensional structure not visible in simple geometric diagnostics. These results establish free space PELMs as experimentally viable multimodal optical feature extractors and motivate future work on embedding design, theoretical modeling, and faster hardware implementations.

Author Contributions

Anushka Kumari contributed to the MNIST and FSDD experiments, optical kernel analysis, feature space diagnostics, and manuscript preparation. Anushree Khisti contributed to the Abalone and Mushroom experiments and participated in the MNIST studies. Abhinav Choube contributed to the experimental setup, hardware alignment, and execution of the experimental analyses. Devansh Satra assisted with manuscript writing and preparation. Srivatsa Murali contributed to the initial experimental setup and system development. Anshuman Kumar supervised the project, guided the research direction, experimental design, theoretical interpretation, and manuscript development.

A Supplementary experimental details

Table 2: Representative hardware and acquisition parameters used in the free-space PELM implementation.

Component	Representative specification	Role
Laser	532 nm green diode, 5 mW class	Coherent illumination
SLM	Phase only Holoeye ERIS class, 1920×1200, 8 μ m pitch	Phase encoding
Optics	4 <i>f</i> style propagation path with iris	Fourier like mixing and first order selection
Camera	CMOS scientific camera, finite bit depth intensity readout	Nonlinear feature detection
Readout	4096 binned spatial channels	ELM feature vector

The iris strongly affects the measured feature quality by suppressing the zero order background and selecting the modulated first order field. Feature normalization minimizes the impact of variations in global laser power and camera response characteristics. The settling time of the SLM needs to be sufficient for the liquid crystal phase state to stabilize following each update; reducing this settling time was shown to negatively affect classification performance. For stable acquisition, it was also necessary to have continuous streaming from the camera, accurate bit depth conversion, timely updates to the SLM buffer, and a methodical sequence for shutting down the hardware.

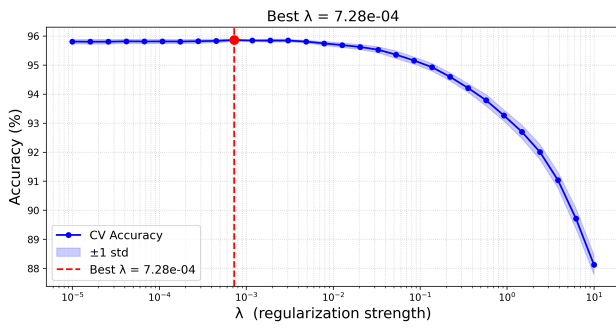
B Supplementary results: ridge parameter optimization

The readout layer is trained using ridge regression,

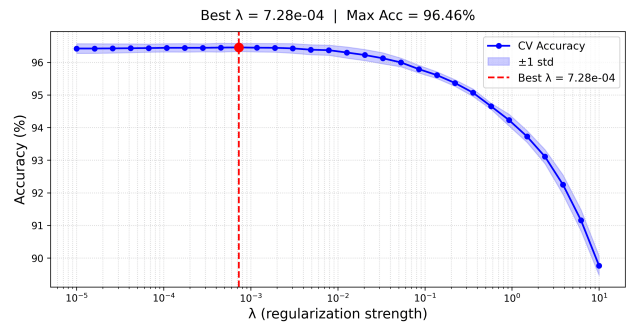
$$\beta = \left(H^\top H + \lambda I \right)^{-1} H^\top T, \quad (20)$$

where $H \in \mathbb{R}^{N \times M}$ is the measured optical feature matrix, T is the target matrix, and λ controls the strength of ℓ_2 regularization. The parameter λ stabilizes the inversion of $H^\top H$ and controls the bias variance tradeoff of the readout. For each dataset and embedding strategy, λ was swept and the optimized performance was reported in the main text. Classification tasks are evaluated using accuracy, while Abalone regression is evaluated using NRMSE.

B.1 MNIST



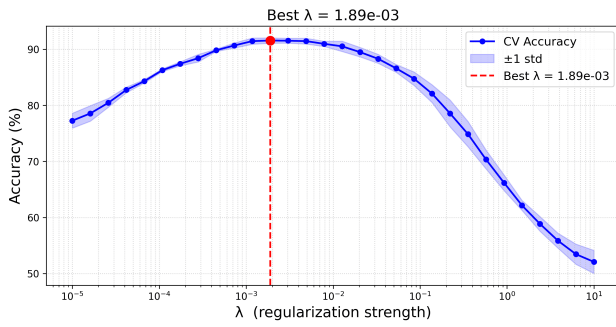
(a) Noise embedding.



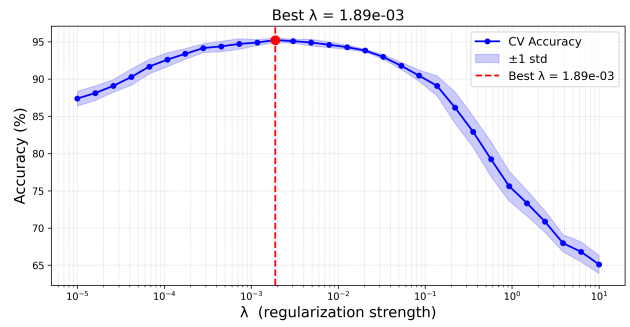
(b) Fourier embedding.

Figure 10: Ridge parameter optimization for MNIST classification. The Fourier embedding gives slightly improved performance, reaching 96.56% accuracy at $\lambda = 7.278 \times 10^{-4}$.

B.2 FSDD spoken digit classification



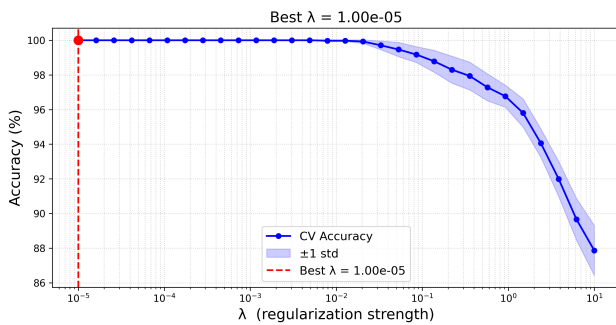
(a) Noise embedding.



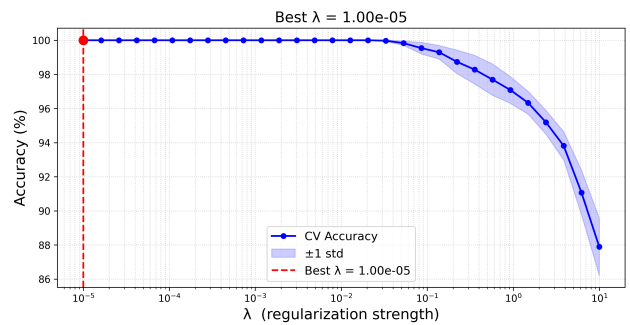
(b) Fourier embedding.

Figure 11: Ridge parameter optimization for FSDD spoken digit classification. The Fourier embedding reaches 95.67% accuracy at $\lambda = 1.887 \times 10^{-3}$.

B.3 Mushroom binary classification



(a) Noise embedding.



(b) Fourier embedding.

Figure 12: Ridge parameter optimization for Mushroom binary classification. Both embeddings operate at saturation and achieve 100.00% classification accuracy.

B.4 Abalone regression

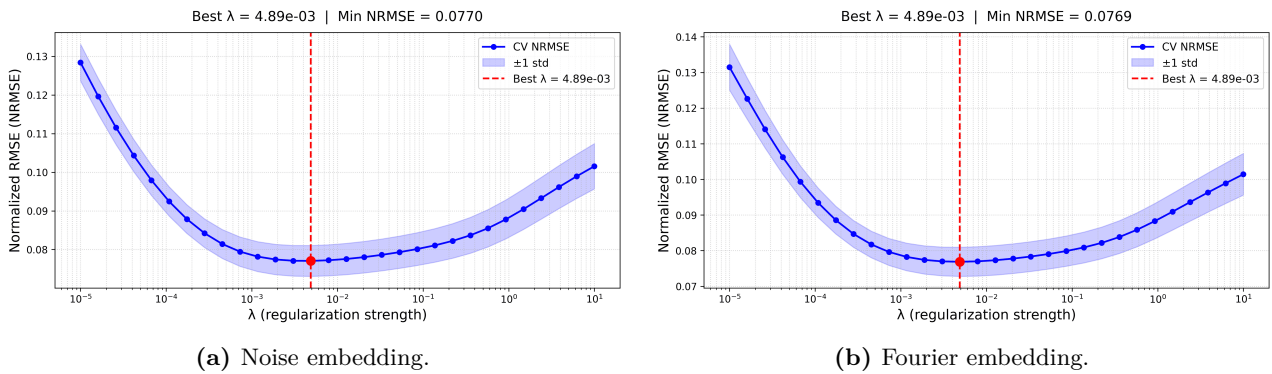


Figure 13: Ridge parameter optimization for Abalone regression. The metric is NRMSE, so lower values correspond to better performance. The optimized values are reported in Table 1.

These sweeps show that optical feature extraction and readout regularization must be considered jointly. The embedding controls the measured feature geometry, while λ controls how strongly the linear readout can exploit weak directions in that feature space.

C Supplementary feature space diagnostics

This section contains the empirical diagnostics for the noise embedding together with additional comparative diagnostics for both embedding strategies beyond those presented in the main text.

C.1 Distance preservation

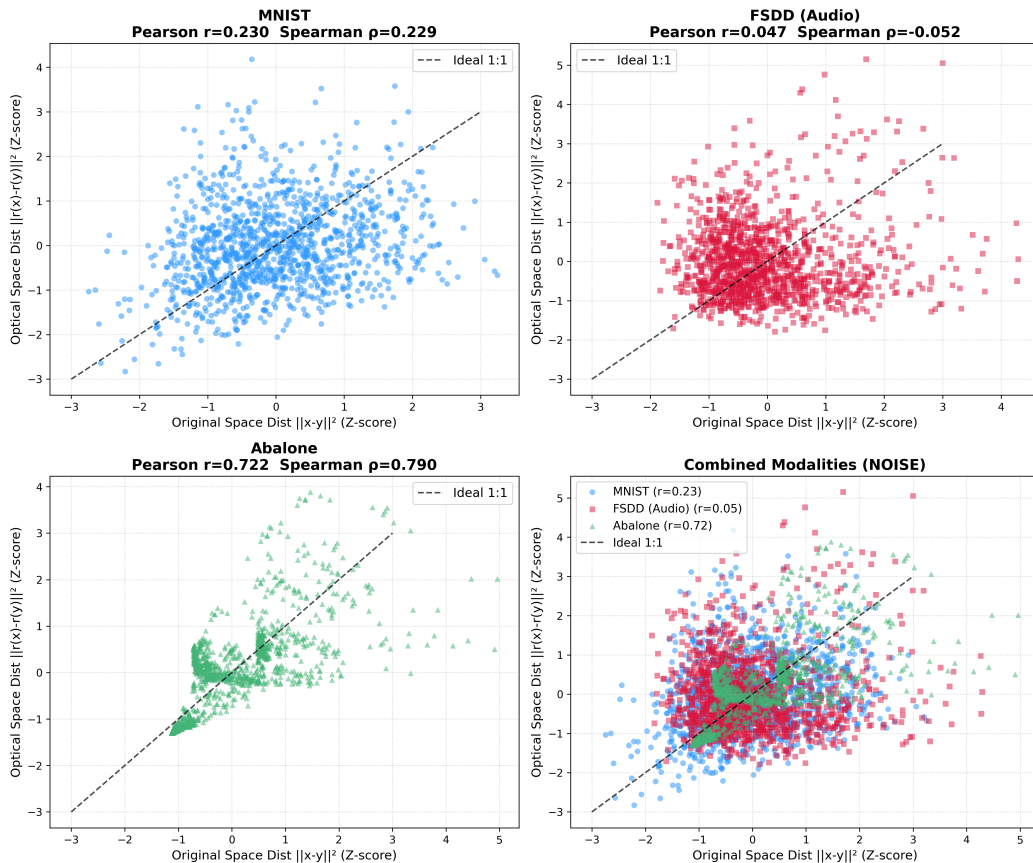


Figure 14: Relative distance preservation diagnostics for Noise Embedding.

C.2 Supplementary Experimental Kernel Fits

To characterize the optical manifold mapping performed by the PELM, we compare the empirical optical kernel against five analytical models. We define the angular separation between L_2 normalized input vectors $\mathbf{x}_i, \mathbf{x}_j$ as $\theta_{ij} = \cos^{-1}(\text{clip}(\mathbf{x}_i^\top \mathbf{x}_j, -1, 1))$. The empirical kernel is estimated as $K_{\text{emp}} = \mathbf{g}_i^\top \mathbf{g}_j$, where \mathbf{g}_i denotes the centered and normalized optical feature vector. In equation of K_{phase} d denotes the dimensionality of the input vectors x .

We evaluate the following theoretical kernel geometries:

$$K_{\text{phase}}(\mathbf{x}_i, \mathbf{x}_j) = 1 + (\mathbf{x}_i^\top \mathbf{x}_j)^2 - \frac{1}{d} \sum_{k=1}^d x_{ik}^2 x_{jk}^2, \quad (21)$$

$$K_{\text{Gauss}}(\theta) = 1 + \cos^2 \theta, \quad (22)$$

$$K_2(\theta) = \frac{\sin \theta + (\pi - \theta) \cos \theta}{\pi}, \quad (23)$$

$$K_1(\theta) = \frac{\pi - \theta}{\pi}, \quad (24)$$

$$K_{\text{RBF}}(\theta) = \exp(-\gamma\theta^2). \quad (25)$$

All theoretical kernels are subsequently double centered prior to comparison with the empirical optical kernel. Kernel agreement is quantified using Pearson correlation coefficient (r) and root mean square error (RMSE) after least squares scaling.

The empirical PELM kernel is binned by input angle θ and compared against the corresponding centered theoretical predictions. Residual and fit quality panels are omitted in the supplementary plots for visual clarity, as the Pearson correlation values are directly reported within the figure legends.

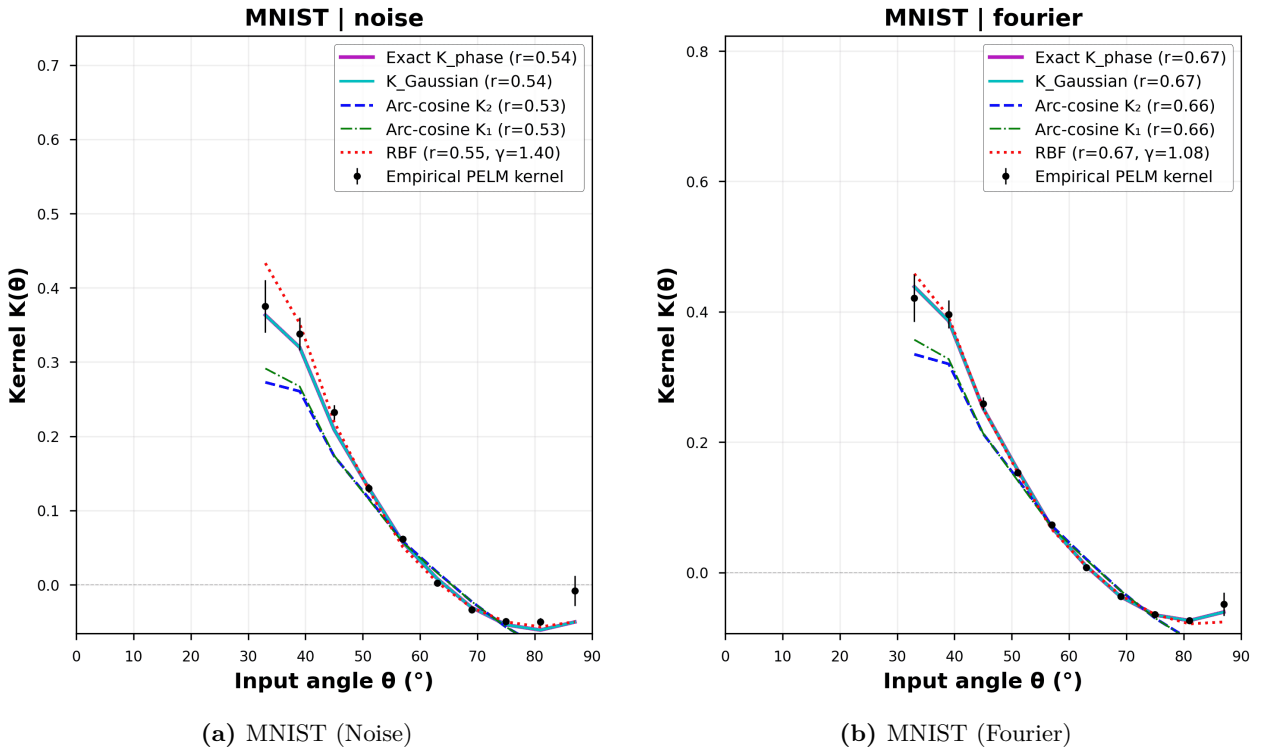
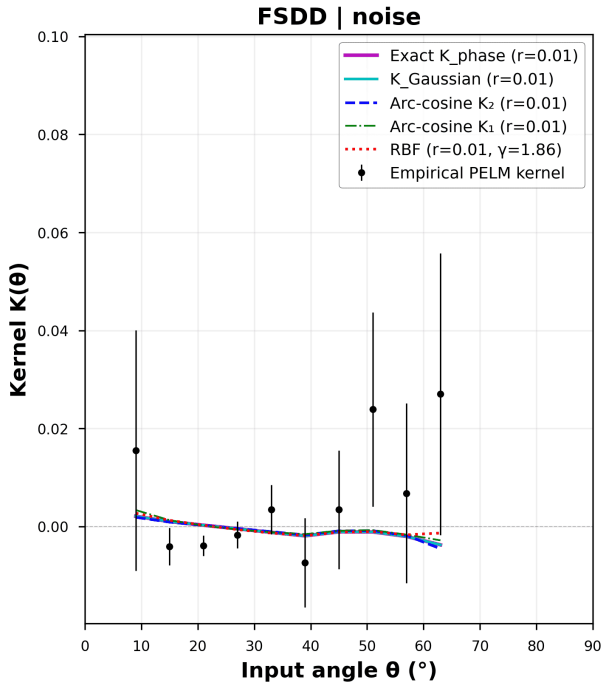
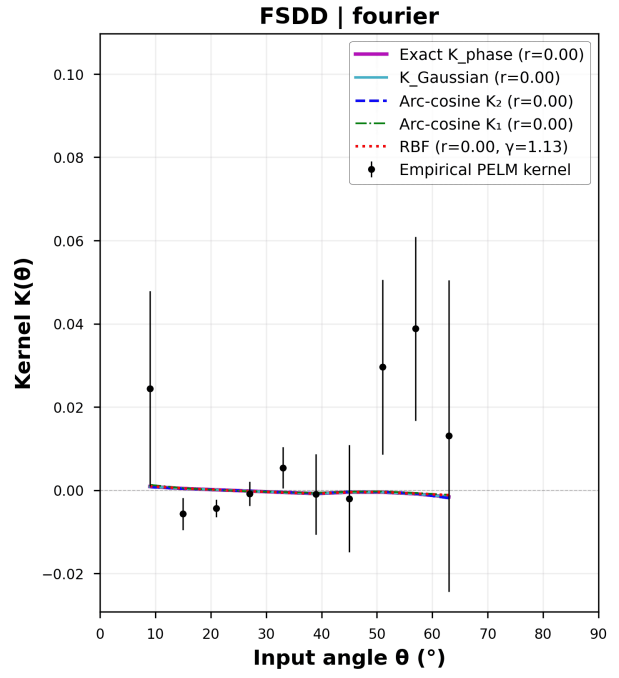


Figure 15: Experimental kernel characterizations for the MNIST dataset.

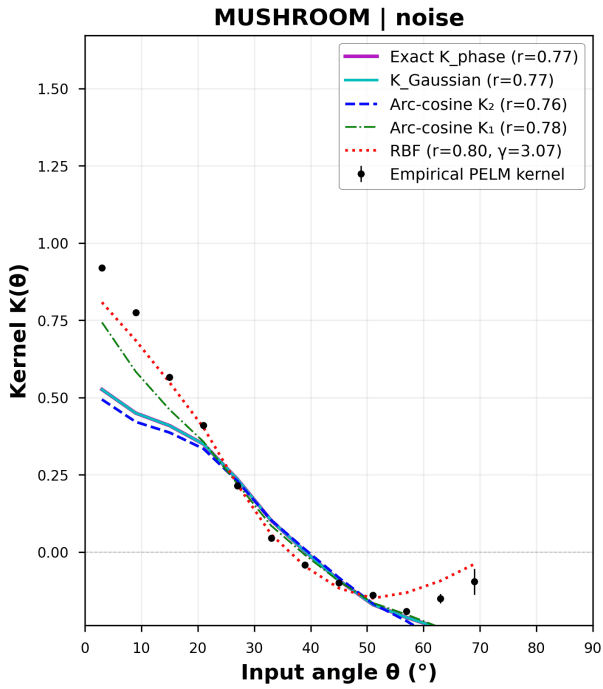


(a) FSDD (Noise)

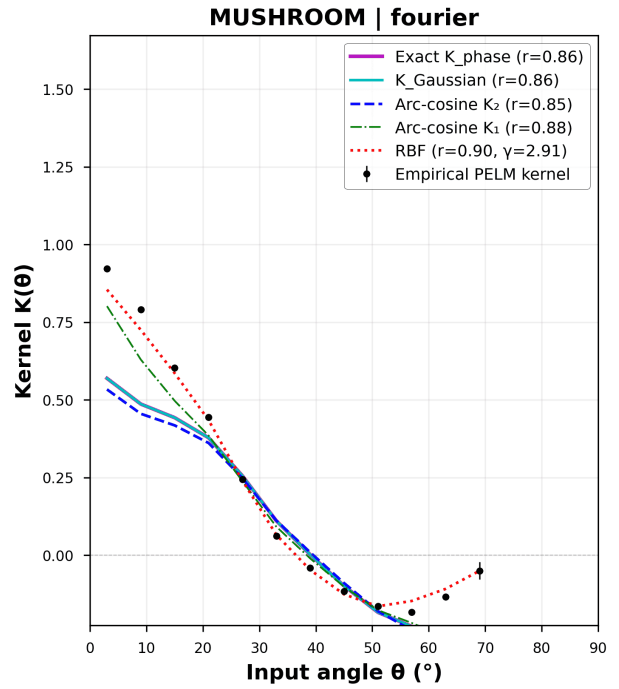


(b) FSDD (Fourier)

Figure 16: Experimental kernel characterizations for the FSDD dataset. Note the flat angular distribution due to the high dimensionality of the audio spectrograms causing distance concentration.



(a) Mushroom (Noise)



(b) Mushroom (Fourier)

Figure 17: Experimental kernel characterizations for the Mushroom dataset.

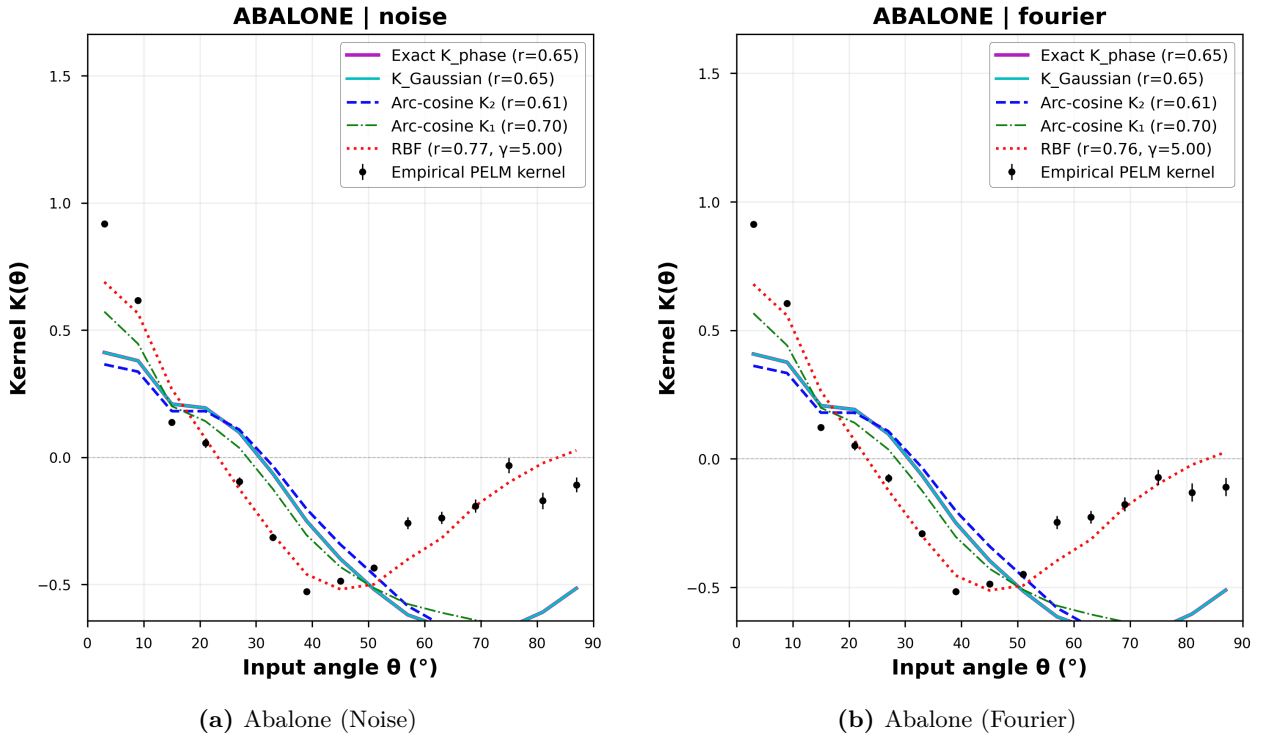


Figure 18: Experimental kernel characterizations for the Abalone dataset.

C.3 Per class separation diagnostics

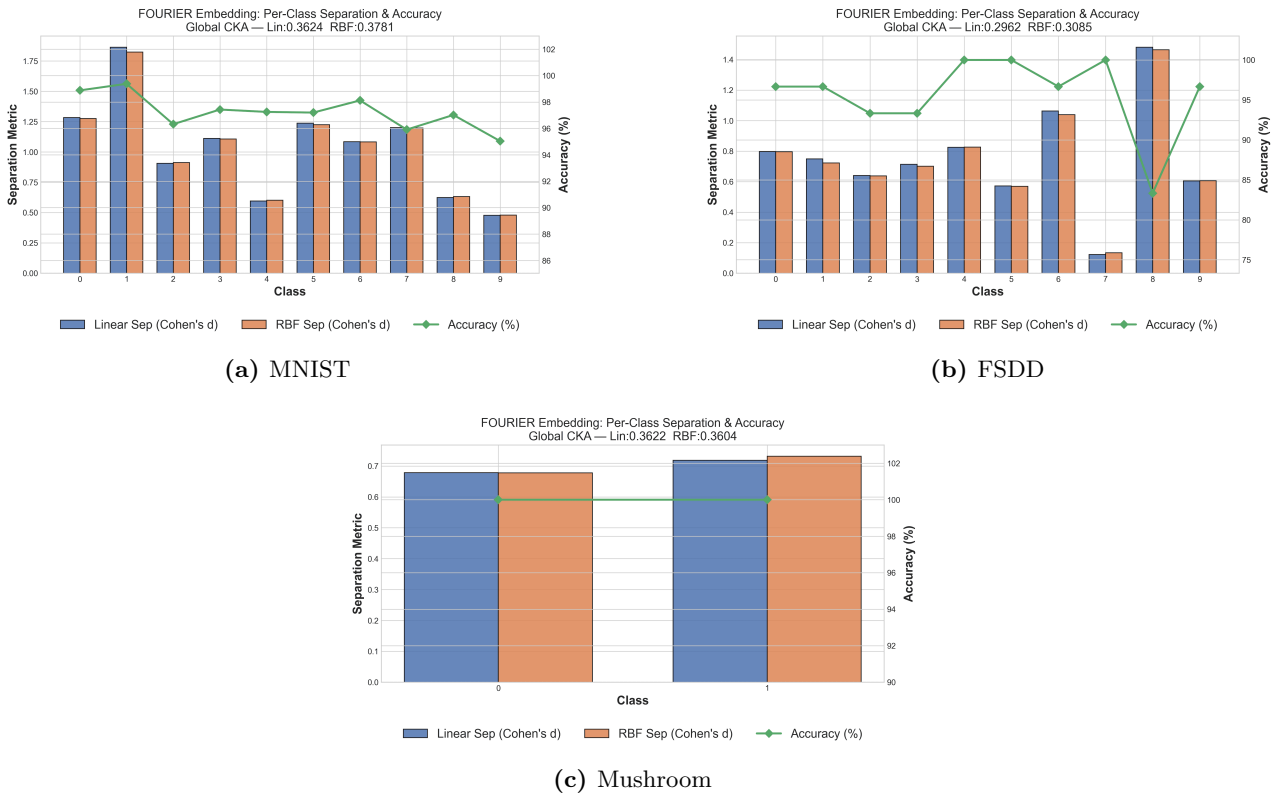
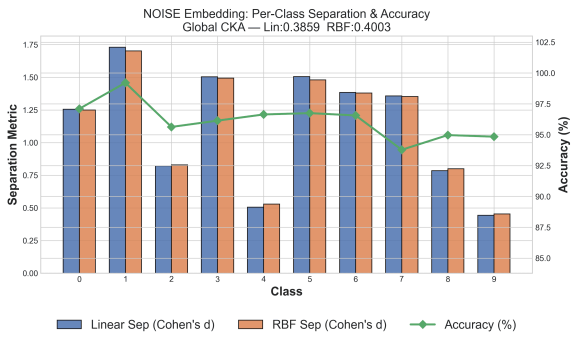
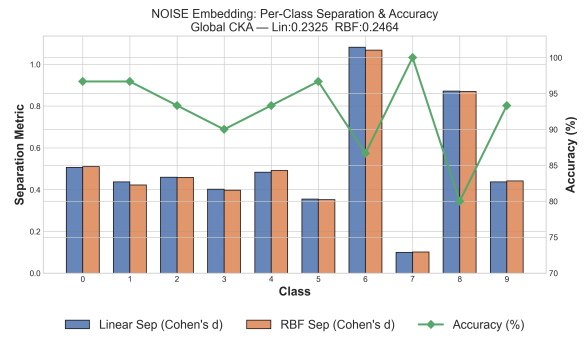


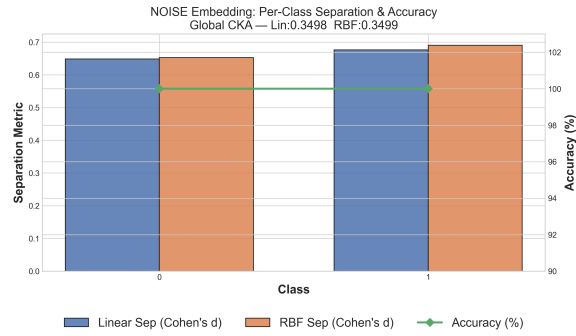
Figure 19: Per class or per target separation diagnostics for the Fourier embedding. MNIST and Mushroom show stronger visible class organization, while FSDD has weaker global separation despite high classification accuracy. Abalone is excluded from these bar plots as categorical class separation metrics (Cohen's d) are inapplicable to continuous regression variables.



(a) MNIST



(b) FSDD



(c) Mushroom

Figure 20: Per class or per target separation diagnostics for the Noise embedding.

C.4 t-SNE visualizations

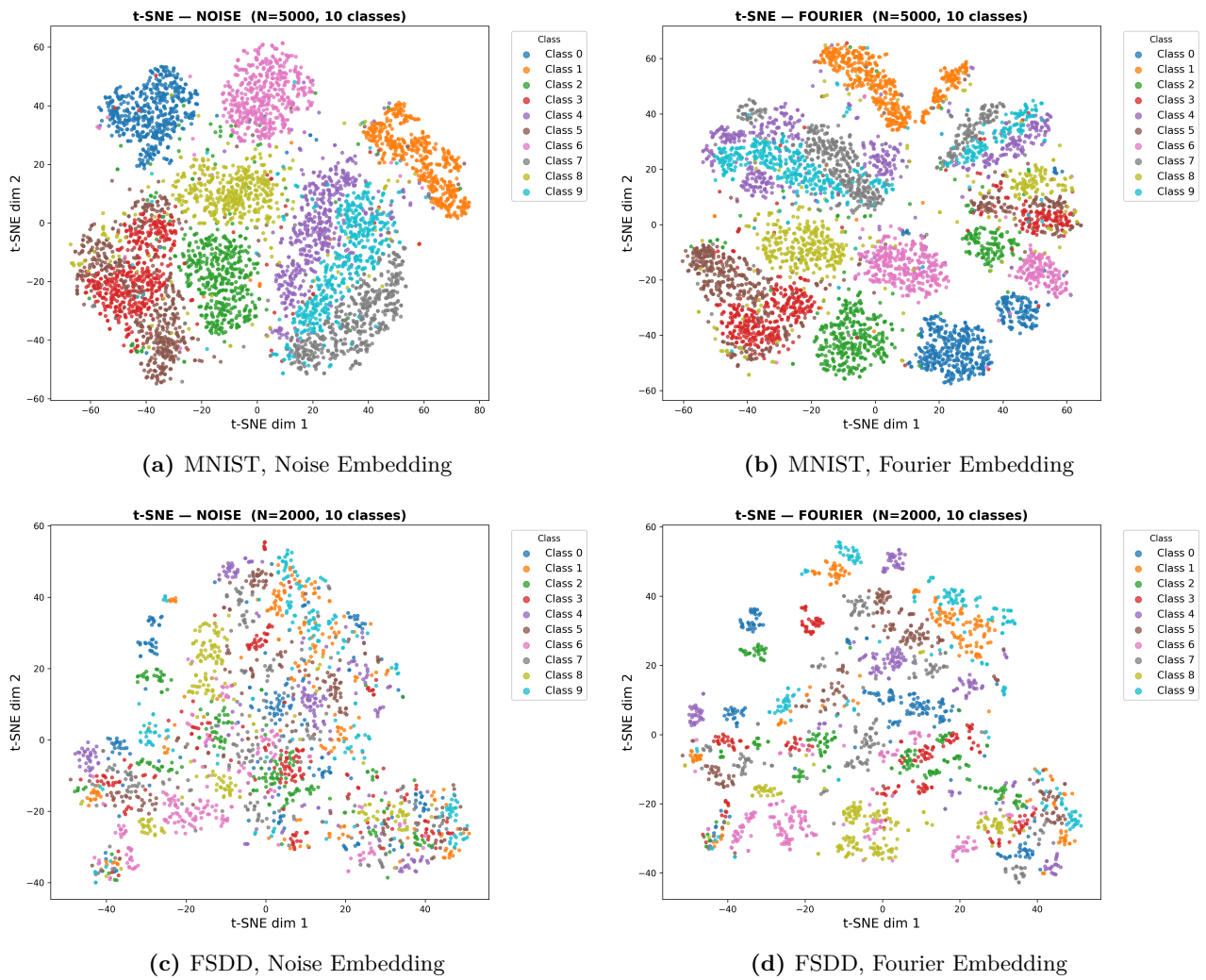
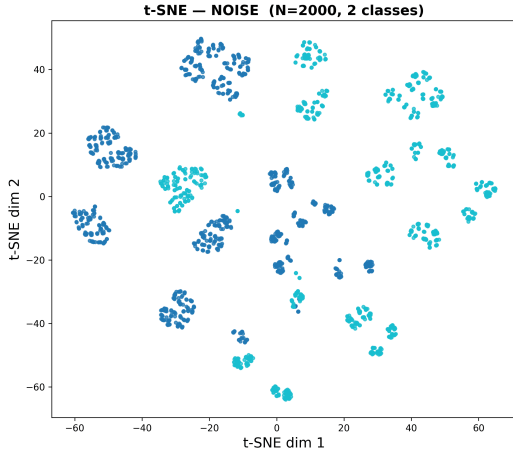
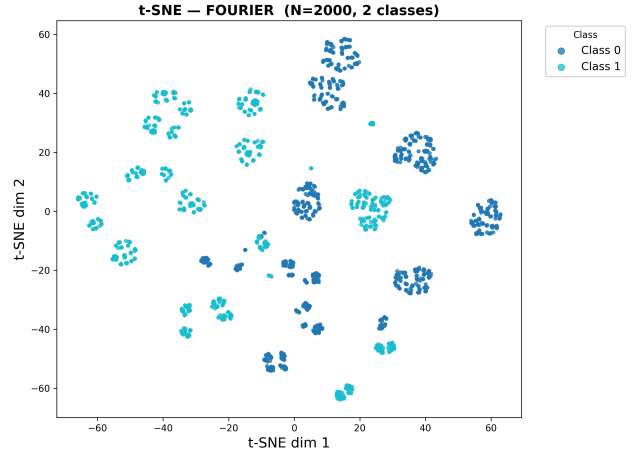


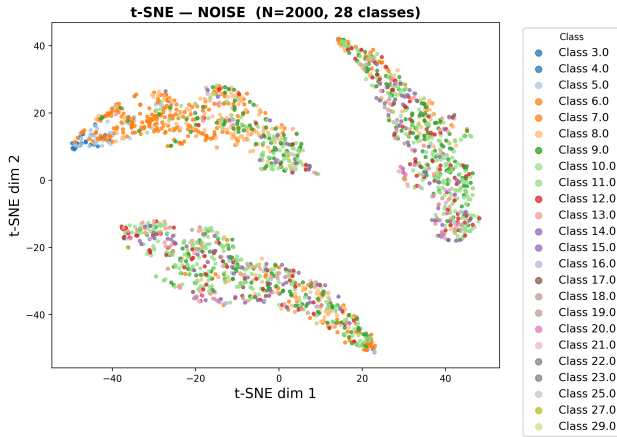
Figure 21: t-SNE visualizations for MNIST and FSDD optical features under both embeddings. The plots are qualitative projections of the measured high dimensional camera features and should be interpreted alongside the quantitative accuracy, distance, and separation diagnostics.



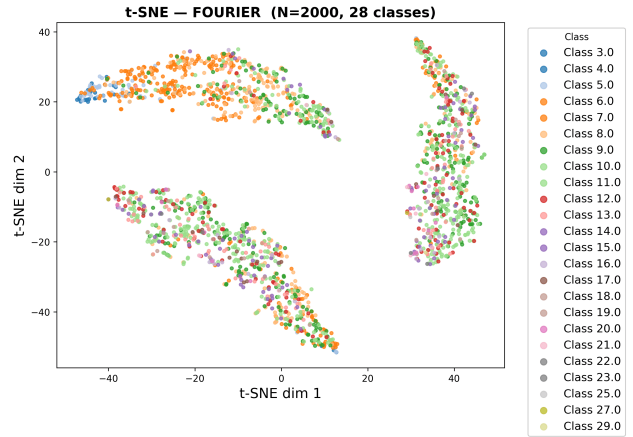
(a) Mushroom, Noise Embedding



(b) Mushroom, Fourier Embedding



(c) Abalone, Noise Embedding

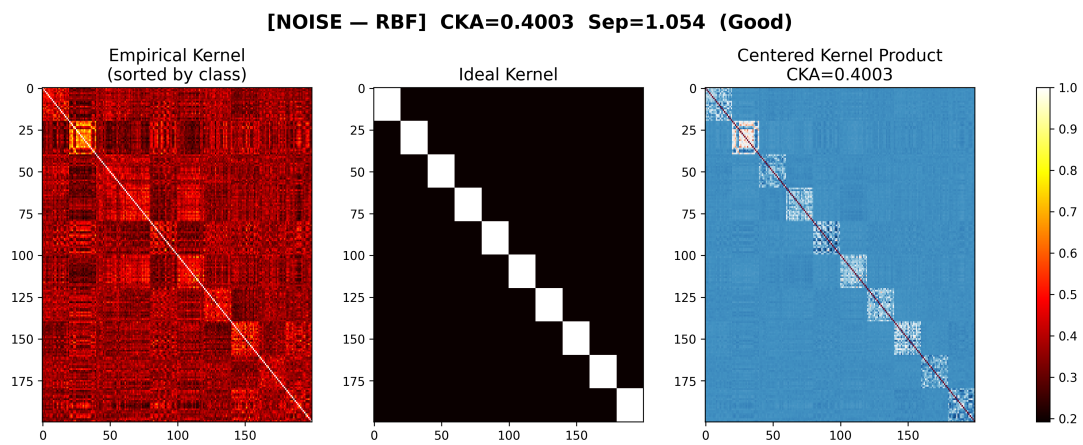


(d) Abalone, Fourier Embedding

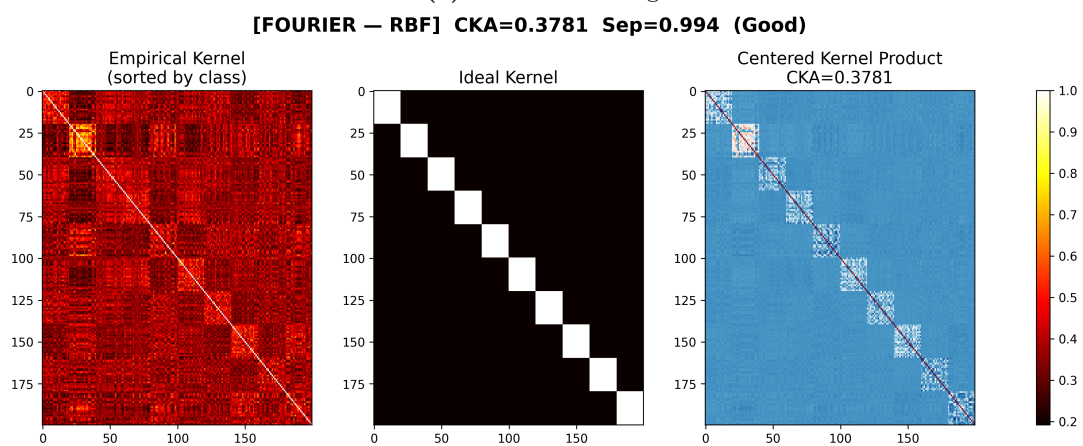
Figure 22: t-SNE visualizations for Mushroom and Abalone optical features under both embeddings. Mushroom forms a more directly separable binary structure, while Abalone forms continuous structures associated with regression targets.

C.5 Empirical kernel matrices

The value labeled “Sep” in the heatmap titles of figs. 23–26 is the ratio of mean between class to within class kernel similarity derived from the empirical RBF kernel matrix. It is a class separation score quantifying how well the optical kernel organizes samples by class, and is distinct from the kernel fit r reported in supp. C.2 and the distance preservation r reported in Sec. 5.2 (Fig. 8 and Supp. C, Fig. 14).

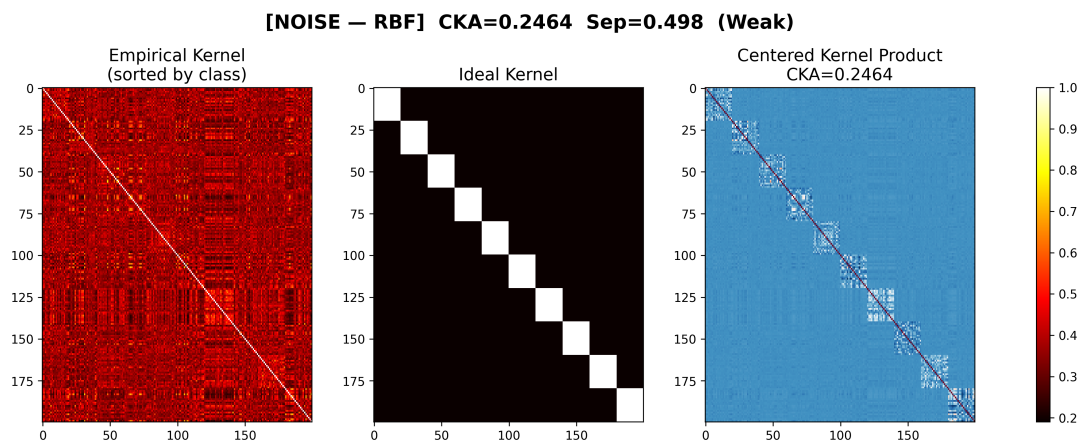


(a) Noise Embedding

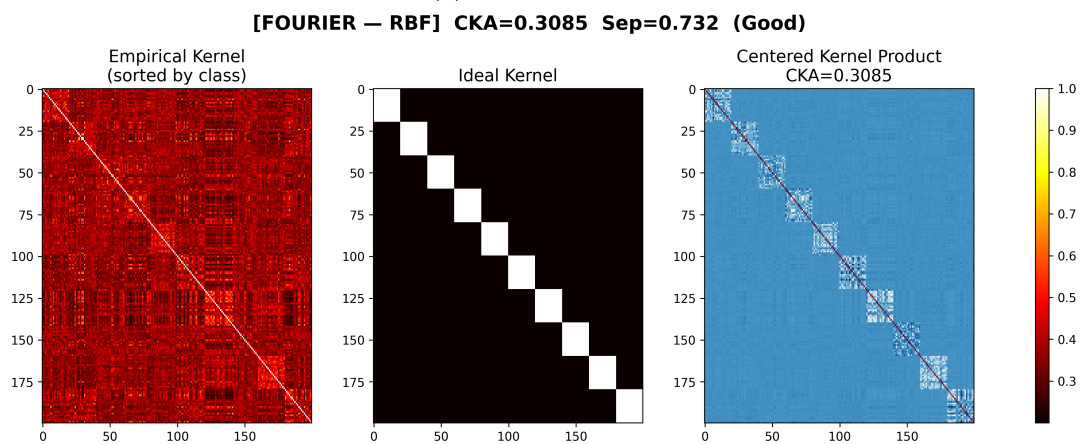


(b) Fourier Embedding

Figure 23: Empirical optical kernel matrices for MNIST using (a) Noise Embedding and (b) Fourier embedding.

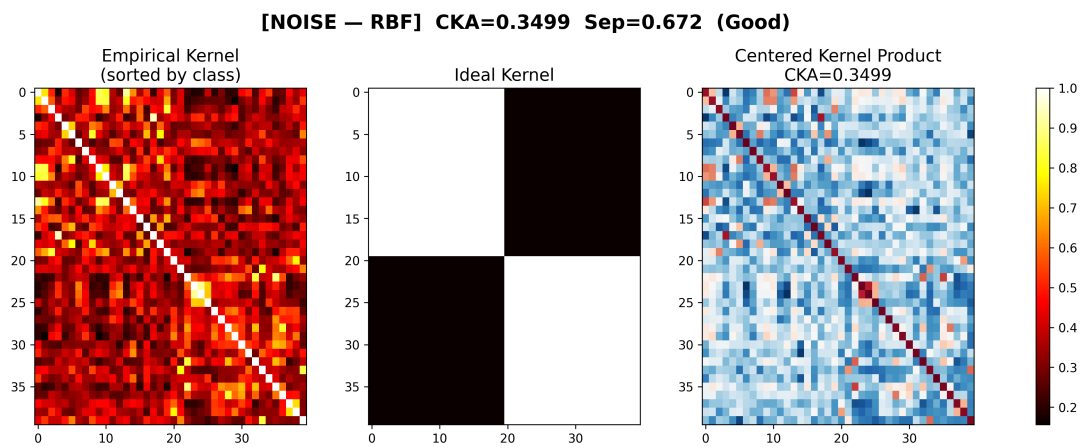


(a) Noise Embedding

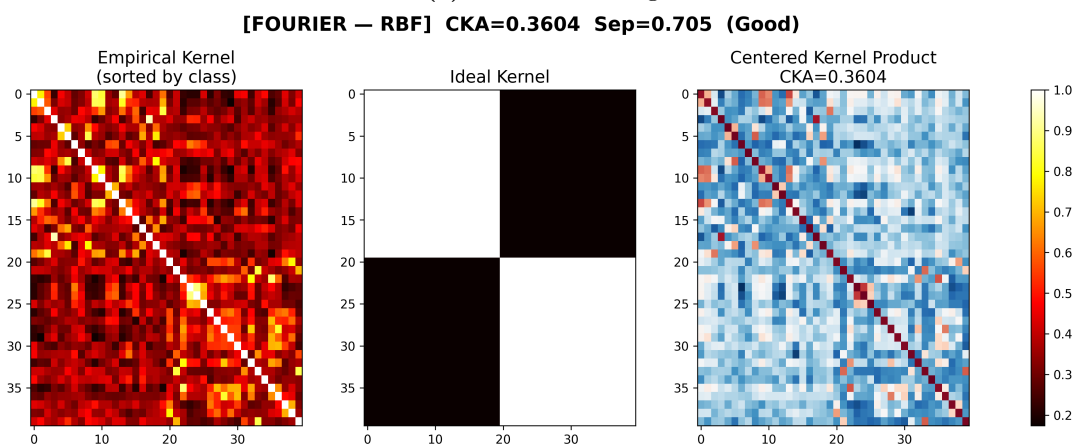


(b) Fourier Embedding

Figure 24: Empirical optical kernel matrices for FSDD using (a) Noise Embedding and (b) Fourier embedding.

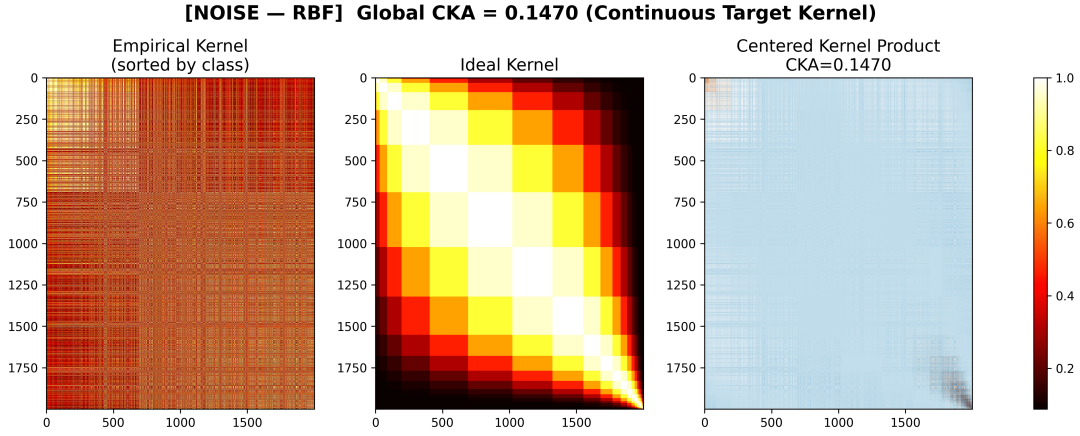


(a) Noise Embedding

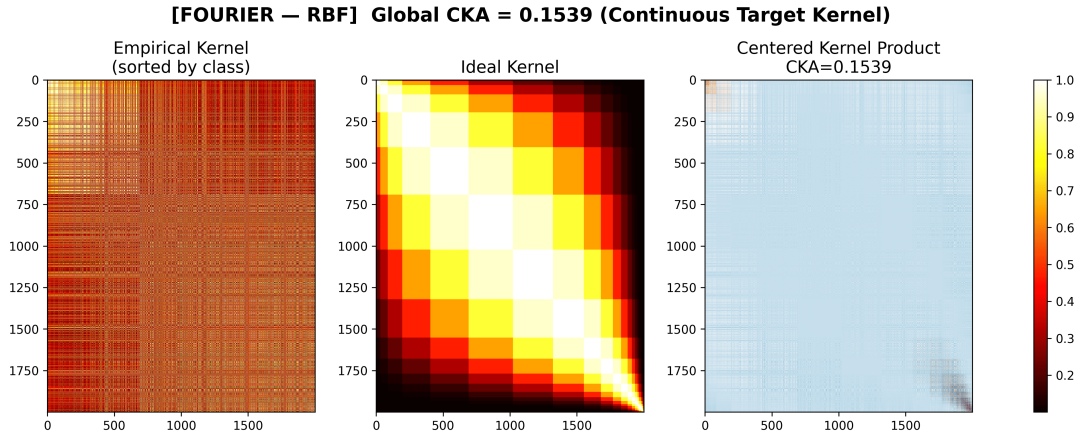


(b) Fourier Embedding

Figure 25: Empirical optical kernel matrices for Mushroom using (a) Noise Embedding and (b) Fourier Embedding



(a) Noise Embedding



(b) Fourier Embedding

Figure 26: Empirical optical kernel matrices for Abalone using (a) Noise Embedding and (b) Fourier Embedding

C.6 Summary of CKA diagnostics

Table 3: Representative completed CKA diagnostics. CKA is interpreted as an encoding diagnostic rather than as a direct predictor of accuracy.

Modality	Embedding	RBF CKA	Performance
MNIST	Noise	0.4003	96.35%
MNIST	Fourier	0.3781	96.56%
FSDD	Noise	0.2464	93.00%
FSDD	Fourier	0.3085	95.67%
Mushroom	Noise	0.3336	100.00%
Mushroom	Fourier	0.3454	100.00%
Abalone	Noise	0.1470	0.0699 NRMSE
Abalone	Fourier	0.1539	0.0704 NRMSE

The CKA diagnostics show that global kernel label alignment varies substantially across modalities. MNIST and Mushroom have stronger global alignment, while FSDD and Abalone have weaker CKA values. This reinforces the main empirical conclusion: the optical feature space need not organize all modalities in the same way. Global alignment, distance preservation, t-SNE structure, and final readout performance should therefore be interpreted together rather than reduced to a single scalar diagnostic.

References

- [1] Michael Reck, Anton Zeilinger, Herbert J. Bernstein, and Philip Bertani. Experimental realization of any discrete unitary operator. *Physical Review Letters*, 73(1):58–61, 1994. doi: 10.1103/PhysRevLett.73.58.
- [2] William R. Clements, Peter C. Humphreys, Benjamin J. Metcalf, W. Steven Kolthammer, and Ian A. Walmsley. Optimal design for universal multiport interferometers. *Optica*, 3(12):1460–1465, 2016. doi: 10.1364/OPTICA.3.001460.
- [3] Yichen Shen, Nicholas C. Harris, Scott Skirlo, Mihika Prabhu, Tom Baehr-Jones, Michael Hochberg, Xin Sun, Shijie Zhao, Hugo Larochelle, Dirk Englund, and Marin Soljačić. Deep learning with coherent nanophotonic circuits. *Nature Photonics*, 11:441–446, 2017. doi: 10.1038/nphoton.2017.93.
- [4] Nicholas C. Harris, Gregory R. Steinbrecher, Mihika Prabhu, Yoav Lahini, Jacob Mower, Darius Bunandar, Changchen Chen, Franco N. C. Wong, Tom Baehr-Jones, Michael Hochberg, Seth Lloyd, and Dirk Englund. Quantum transport simulations in a programmable nanophotonic processor. *Nature Photonics*, 11:447–452, 2017. doi: 10.1038/nphoton.2017.95.
- [5] Wim Bogaerts, Daniel Pérez, José Capmany, David A. B. Miller, Joyce Poon, Dirk Englund, Francesco Morichetti, and Andrea Melloni. Programmable photonic circuits. *Nature*, 586(7828): 207–216, 2020. doi: 10.1038/s41586-020-2764-0.
- [6] Xing Lin, Yair Rivenson, Nezih T. Yardimci, Muhammed Veli, Yi Luo, Mona Jarrahi, and Aydogan Ozcan. All-optical machine learning using diffractive deep neural networks. *Science*, 361(6406):1004–1008, 2018. doi: 10.1126/science.aat8084.
- [7] Deniz Mengu, Yi Luo, Yair Rivenson, and Aydogan Ozcan. Analysis of diffractive optical neural networks and their integration with electronic neural networks. *IEEE Journal of Selected Topics in Quantum Electronics*, 26(1):8732486, 2020. doi: 10.1109/JSTQE.2019.2921376.
- [8] Tao Yan, Rui Yang, Ziyang Zheng, Xing Lin, Hongkai Xiong, and Qionghai Dai. All-optical graph representation learning using integrated diffractive photonic computing units. *Science Advances*, 8(24):eabn7630, 2022. doi: 10.1126/sciadv.abn7630.
- [9] Yuyao Huang, Tingzhao Fu, Honghao Huang, Sigang Yang, and Hongwei Chen. Sophisticated deep learning with on-chip optical diffractive tensor processing. *Photonics Research*, 11(6): 1125–1138, 2023. doi: 10.1364/PRJ.484662.
- [10] Carlos Rios, Matthias Stegmaier, Peiman Hosseini, Dandan Wang, Thomas Scherer, C. David Wright, Harish Bhaskaran, and Wolfram H. P. Pernice. Integrated all-photonic non-volatile multi-level memory. *Nature Photonics*, 9:725–732, 2015. doi: 10.1038/nphoton.2015.182.
- [11] Johannes Feldmann, Nathan Youngblood, C. David Wright, Harish Bhaskaran, and Wolfram H. P. Pernice. All-optical spiking neurosynaptic networks with self-learning capabilities. *Nature*, 569:208–214, 2019. doi: 10.1038/s41586-019-1157-8.
- [12] Johannes Feldmann, Nathan Youngblood, Maxim Karpov, Helge Gehring, Xuan Li, Maik Stappers, Manuel Le Gallo, Xin Fu, Anton Lukashchuk, Arslan S. Raja, Junqiu Liu, C. David Wright, Abu Sebastian, Tobias J. Kippenberg, Wolfram H. P. Pernice, and Harish Bhaskaran. Parallel convolutional processing using an integrated photonic tensor core. *Nature*, 589(7840):52–58, 2021. doi: 10.1038/s41586-020-03070-1.
- [13] Zhongjin Lin, Bhavin J. Shastri, Shangxuan Yu, Jingxiang Song, Yuntao Zhu, Arman Safarnejadian, Wangning Cai, Yanmei Lin, Wei Ke, Mustafa Hammood, Tianye Wang, Mengyue Xu, Zibo Zheng, Mohammed Al-Qadasi, Omid Esmaeeli, Mohamed Rahim, Grzegorz Pakulski, Jens Schmid, Pedro Barrios, Weihong Jiang, Hugh Morison, Matthew Mitchell, Xun Guan, Nicolas

- A. F. Jaeger, Leslie A. Rusch, Sudip Shekhar, Wei Shi, Siyuan Yu, Xinlun Cai, and Lukas Chrostowski. 120 GOPS photonic tensor core in thin-film lithium niobate for inference and in situ training. *Nature Communications*, 15(1):9081, 2024. doi: 10.1038/s41467-024-53261-x.
- [14] Daniel Brunner, Miguel C. Soriano, Claudio R. Mirasso, and Ingo Fischer. Parallel photonic information processing at gigabyte per second data rates using transient states. *Nature Communications*, 4:1364, 2013. doi: 10.1038/ncomms2368.
- [15] Upendra Paudel, M. Luengo-Kovac, Joseph Pilawa, Timothy J. Shaw, and George C. Valley. Classification of time-domain waveforms using a speckle-based optical reservoir computer. *Optics Express*, 28(2):1225–1237, 2020. doi: 10.1364/OE.28.001225.
- [16] Mushegh Rafayelyan, Jing Dong, Yiqing Tan, Florent Krzakala, and Sylvain Gigan. Large-scale optical reservoir computing for spatiotemporal chaotic systems prediction. *Physical Review X*, 10:041037, 2020. doi: 10.1103/PhysRevX.10.041037.
- [17] Tyler W. Hughes, Momchil Minkov, Yu Shi, and Shanhui Fan. Training of photonic neural networks through in situ backpropagation and gradient measurement. *Optica*, 5(7):864–871, 2018. doi: 10.1364/OPTICA.5.000864.
- [18] Jiaqi Gu, Hanqing Zhu, Chenghao Feng, Zixuan Jiang, Ray T. Chen, and David Z. Pan. L2ight: Enabling on-chip learning for optical neural networks via efficient in-situ subspace optimization. In *Advances in Neural Information Processing Systems*, volume 34, 2021. URL <https://proceedings.neurips.cc/paper/2021/hash/48aedb8880cab8c45637abc7493ecddd-Abstract.html>.
- [19] Junwei Cheng, Chaoran Huang, Jialong Zhang, Bo Wu, Wenkai Zhang, Xinyu Liu, Jiahui Zhang, Yiyi Tang, Hailong Zhou, Qiming Zhang, Min Gu, Jianji Dong, and Xinliang Zhang. Multimodal deep learning using on-chip diffractive optics with in situ training capability. *Nature Communications*, 15(1):6189, 2024. doi: 10.1038/s41467-024-50677-3. URL <https://doi.org/10.1038/s41467-024-50677-3>.
- [20] Gordon Wetzstein, Aydogan Ozcan, Sylvain Gigan, Shanhui Fan, Dirk Englund, Marin Soljačić, Cornelia Denz, David A. B. Miller, and Demetri Psaltis. Inference in artificial intelligence with deep optics and photonics. *Nature*, 588:39–47, 2020. doi: 10.1038/s41586-020-2973-6.
- [21] Bhavin J. Shastri, Alexander N. Tait, Thomas Ferreira de Lima, Wolfram H. P. Pernice, Harish Bhaskaran, C. David Wright, and Paul R. Prucnal. Photonics for artificial intelligence and neuromorphic computing. *Nature Photonics*, 15:102–114, 2021. doi: 10.1038/s41566-020-00754-y.
- [22] Guang-Bin Huang, Qin-Yu Zhu, and Chee-Kheong Siew. Extreme learning machine: theory and applications. *Neurocomputing*, 70(1–3):489–501, 2006. doi: 10.1016/j.neucom.2005.12.126.
- [23] Davide Pierangeli, Giulia Marcucci, and Claudio Conti. Photonic extreme learning machine by free-space optical propagation. *Photonics Research*, 9(8):1446–1454, 2021. doi: 10.1364/PRJ.423531.
- [24] Zohar Jackson. Free spoken digit dataset (fsdd). <https://github.com/Jakobovski/free-spoken-digit-dataset>, 2017. Accessed: 2026-05-21.
- [25] Steven B. Davis and Paul Mermelstein. Comparison of parametric representations for monosyllabic word recognition in continuously spoken sentences. *IEEE Transactions on Acoustics, Speech, and Signal Processing*, 28(4):357–366, 1980. doi: 10.1109/TASSP.1980.1163420.
- [26] UCI Machine Learning Repository. Mushroom dataset. <https://archive.ics.uci.edu/ml/datasets/mushroom>, . Accessed: 2026-05-21.
- [27] UCI Machine Learning Repository. Abalone dataset. <https://archive.ics.uci.edu/ml/datasets/abalone>, . Accessed: 2026-05-21.

- [28] Bernhard Schölkopf and Alexander J. Smola. *Learning with Kernels: Support Vector Machines, Regularization, Optimization, and Beyond*. MIT Press, Cambridge, MA, 2002. ISBN 9780262194754.
- [29] Nello Cristianini, John Shawe-Taylor, André Elisseeff, and Jaz S. Kandola. On kernel-target alignment. In *Advances in Neural Information Processing Systems*, volume 14, 2001. URL https://proceedings.neurips.cc/paper_files/paper/2001/hash/1f71e393b3809197ed66df836fe833e5-Abstract.html.
- [30] Simon Kornblith, Mohammad Norouzi, Honglak Lee, and Geoffrey Hinton. Similarity of neural network representations revisited. In *Proceedings of the 36th International Conference on Machine Learning*, volume 97 of *Proceedings of Machine Learning Research*, pages 3519–3529. PMLR, 2019. URL <https://proceedings.mlr.press/v97/kornblith19a.html>.
- [31] Laurens van der Maaten and Geoffrey Hinton. Visualizing data using t-SNE. *Journal of Machine Learning Research*, 9(86):2579–2605, 2008. URL <http://jmlr.org/papers/v9/vandermaaten08a.html>.